UNIVERSITY OF OKLAHOMA
GRADUATE COLLEGE

LIMITATIONS AND EVALUATION OF THE LINEAR ASSUMPTION ON ANTENNA DESIGN

A THESIS
SUBMITTED TO THE GRADUATE FACULTY
in partial fulfillment of the requirements for the
Degree of
MASTER OF SCIENCE

By

CLAYTON BLOSSER
Norman, Oklahoma
2022

LIMITATIONS AND EVALUATION OF THE LINEAR ASSUMPTION ON ANTENNA DESIGN

A THESIS APPROVED FOR THE
SCHOOL OF ELECTRICAL AND COMPUTER ENGINEERING

BY THE COMMITTEE CONSISTING OF

Dr. Jessica Ruyle, Chair

Dr. K.C. Kerby-Patel

Dr. Hjalti Sigmarsson

Acknowledgments

First, I would like to thank Dr. Jessica Ruyle for her counsel in both academic and personal matters, support as an advisor, and fostering the researcher within all her students, Ashley Cook for encouraging me to try out research, and Dr. K.C. Kerby-Patel and Dr. Kurt Schab for their mentorship and support, and their fresh take on research.

Second, I would like to thank Stephen Bass for his friendship and support, and showing me how to think like a researcher, Kyle Kanaly for his candid friendship and helping me learn how to take care of myself, and Eric Wells, Patrick O'Connor-Lynch, and Jon Knowles for their camaraderie and real-time empathy.

Third, I would like to thank my little brother for being my first and best friend and an advocate, my mother and father for their unending support and love only parents could offer, my grandfather for encouraging science and thinking, and my uncle and grandmother who made me who I am today and sadly could not see me achieve this.

Finally, I would like to thank my beautiful wife, my love and confidant, without whom I would succeed nothing, and to my hounds, Ranger, Josie, Noodle, Pumpkin, and Nic, who possess more emotional wisdom than any human could.

Contents

List of Tables

List of Figures

Abstract

A common assumption made by antenna engineers is to consider a system to be linear and time-invariant (LTI). This assumption is incredibly powerful and has enabled a century of advancements, but consequently has perhaps made electrical engineering too reliant upon it. There are multiple cases of fundamental limits being circumvented by including non-LTI devices and analysis. Additionally, there are limitations of some systems that are not well understood or avoided as a subject due to their non-LTI nature. Exotic antennas are attractive to complex, modern communication systems, but they are effectively useless if they cannot be deployed in practical settings after design sequences - as is sometimes the case in the presence of potentially nonlinear devices. Therefore, this work provides insight into the limitations of non-LTI analysis for antenna engineering and the trade-offs of some antennas that are erroneously capable of nonlinear behavior. Doing so will help shed light on the ramifications of casually making the LTI assumption and methods to better understand such antennas.

Chapter 1

Introduction

1.1 Motivation

Scientists and researchers regularly make assumptions on problems in order to make them manageable and comprehensible. However, it is often that as the years pass these assumptions either no longer have to be made due to scientific or technological advances, were incorrect to make to begin with, or limited the possibilities of the solution to the problem. Linearity and time-invariance (LTI) are frequent assumptions made by electrical engineers to make problems manageable. While there was good reason to become rooted in the LTI assumption, perhaps it is too limiting to antenna engineers today. The LTI assumption helps immensely in a few, key ways. One is that it simplifies calculations and models, and has historically been a necessary step for limited computation power. Second, the LTI assumption allows for unhindered Fourier Analysis to permit frequency domain representations - crucial to modern electrical signal and system analysis. Third, many systems work best when they operate linearly, although this is in part to assumptions made when the system was designed. Therefore, enforcing linearity in a design simultaneously makes the system more effective and LTI analysis an accurate simplification. While this attractive assumption has propelled electrical engineering for nearly a century, it could benefit to remove it in some situations.

Interestingly enough, non-LTI antennas were actually common place in the earlier days of wireless transmission. Heinrich Hertz utilized spark-gap sources for some of his work on establishing antenna theory [1]. Additionally, utilization of direct antenna modulation (DAM) and parametric amplification were thoroughly explored in the first half of the twentieth century. It wasn't until the invention of the BJT that these methods became obsolete and fell to the wayside [2]. The advancement of semiconductors combined with a need for steady-state systems to permit communication beyond Morse code led to the inclusion of the LTI assumption, and electrical engineers seldom looked back.

Computational advancements, numerical methods, and improved RF components make dropping the LTI assumption appealing. So much so, that there are already some contemporary applications of non-LTI systems. An example are engineers that have gone back to parametric amplification. Parametric amplification is used today in sub-mm wave applications as the amplified up-conversion aids in mixing into the hundreds of gigahertz [3]. Additionally, parametric amplification has been used in challenging the Bode-Fano criteria for matching [4]. Permitting time-variance has proved useful in challenging bandwidth constraints as well. Revisiting DAM has shown that the limitations of electrically small antenna's (ESA) Q, as described by Chu's limit, could be circumvented by increasing the bandwidth past what should be possible [5], [6]. Additionally, temporally switching the properties of a transmission line has also shown potential in overcoming the Bode-Fano limit [7]. Switching is not just limited to bandwidth improvements, as spatio-temporal modulation has been used to break reciprocity without the use of magnetic materials in [8], [9]. Even something as simple as a nonlinear inductor has been theorized to overcome bandwidth limitations in ESAs [10]. For antenna engineers, these prospects and more invite new possibilities, like: efficient and high bandwidth ESAs, non-reciprocal antennas, and highly pattern reconfigurable antennas.

In order to explore this avenue, engineers need to better understand the limitations of non-LTI systems. This thesis helps by reviewing non-LTI simulation methods and a commercial implementation in Chapter 2, deriving a new power-balance relationship for time-varying resistances and evaluating reactive power in a non-LTI system from an RF perspective in Chapter 3, quantifying the linear limitations of a popular frequency reconfigurability technique utilizing varactor diodes in Chapter 4, and exploring the nonlinear characteristics of ferro-magnetic substrates in Chapter 5.

1.2 Simulation Methods

While there are numerous numerical methods that can handle electromagnetic waves, the number that can handle non-LTI systems is not as great, and the number that are efficient and accurate enough to be a viable solution is even smaller. The most popular at the time of this writing is the Finite-Difference Time-Domain method (FDTD). FDTD is well documented and has been evolving over the past several decades making sure to keep up with modern RF design demands. FDTD is robust as it can handle both time varying and nonlinear elements, the former natively and the latter with little modification [11]. Moreover, it can handle lumped components and includes a litany of tools just for antenna simulation [11]–[13]. The subject of Chapter 2 is not to merely review the basics of FDTD, but also to assess major sources of error in relation to the only major commercial electromagnetic solver whose primary function is FDTD, Remcom’s Xfdtd. This will serve to inspect the reliability of the software, both for LTI and non-LTI cases.

While FDTD is perhaps the most robust solver with non-LTI capabilities, there are other worthwhile avenues with their own strengths and weaknesses to be considered. Volterra is perhaps the most commonly used for non-LTI systems, but due to it's simplicity and wide implementation will be over-looked here. One that is considered in Chapter 2 is Conversion Matrices (CM). CM is a port based analysis technique that permits time-varying systems and large signal, nonlinear analysis [14], [15]. Since the method is based on the Fourier series its usage integrates well into current electrical engineering analysis. Another method that Chapter 2 explains is harmonic balance (HB). HB handles nonlinear circuits by partitioning the linear and nonlinear portions into separate problems and connects them via a port [14]. HB has seen plenty of improvements in recent decades, as its' ability to incorporate any root-finding numerical method into classic network problems makes it very versatile and accurate. CM and HB have been used in conjunction with a full wave solver and a single lumped element to simulation a non-LTI antenna in [16] and [17]. CM has gone on to be used to simulate an arbitrary number of discretized elements within a method of moments impedance matrix in [15], going as far to simulate an entire sphere of time-modulated conductivity. Between these three methods, any non-LTI problem is surmountable, and understanding them is key to non-LTI design.

1.3 Reactive Power and Harmonic Power-Balance Relations

Power conservation is a crucial governing constraint on physical systems. However, it can often fall short of meaningfully describing a certain system. One particular system that has benefited from additional constraining equations are time-varying reactances who can appear as real power at harmonics. Manley and Rowe developed the Manley-Rowe power balance relations to describe the power at other frequencies in terms of ratios of the harmonics' frequencies when a pumped, nonlinear reactance is present in a circuit [18]. Manley and Rowe were able to show that these reactances can appear as negative resistances, thus amplifying any excitation signals already present in the system - this is the premise of parametric amplifiers. They extended their analysis to real valued loads, like time-varying resistors, but their analysis was not insightful for two reasons: their derivation was merely a sum weighted by the harmonic integer, and the definition of reactive power was different from today's [19]. Therefore, Chapter 3 derives a more thorough relationship to better relate reactive power at different harmonics, and investigates both the old and new reactive power definitions to gain a better understanding of the lack of conservation, and to more generally aid in non-LTI power analysis. The results here will help to enlighten how reactive power can be handled and the limitations of the current understanding.

1.4 Limitations of Varactor-Based Reconfigurable Antennas

Frequency agile antennas are increasingly popular in an ever-crowding Radio Frequency (RF) spectrum. These antennas can alter their pattern, polarization, or operating frequencies, and accomplish this through a multitude of methods [20]. Using variable reactances is one such method, and variable capacitance varactor diodes (varactors) are a common tool uses to realize these antennas. While there are many reasons that these components are attractive for reconfigurable antennas, there are drawbacks that, to this point, have not been sufficiently characterized and understood - especially their nonlinear nature and power handling. It is possible for varactors to generate harmonics that will radiate and pollute the spectrum [21], [22]. However, one particular drawback to these analysis is a lack of amplifier harmonic distortion measurement. In [22] the authors did use a low pass filter in order to limit the impacts of the signal generator's harmonics, but did not discuss or mitigate their affects further. While a filter is a necessary addition it cannot have ideal stop-band rejection, and the harmonics that pass through need to be measured. In [21] the harmonics were completely neglected and an additional preamplifier was used. This analysis appropriately characterizes the harmonics from other sources with a control measurement to guarantee the phenomenon originate from the devices under test. Another significant effect of utilizing nonlinear devices that has not been thoroughly characterized is the possible impact on an antenna's impedance. It has been shown that varactors will change their impedance as a function of input RF power [23]. Therefore, it is reasonable to assume that with a high enough RF power the match of an antenna with the system will degrade. Chapter 4 looks into varactor-based reconfigurable antenna design to review and affirm what is understood about radiated intermodulation distortion, quantify match degradation in antennas due to larger RF voltages on varactors, and compare these phenomenon against that of another reconfigurable antenna and control case.

1.5 Limitations of Magneto-Dielectric Substrates

Patch antennas are a great solution to many communication problems, but like all radiators they come with strengths and weaknesses. One particular issue with patch antennas are their incredibly narrow bandwidths. However, Hansen showed that using a magneto-dielectric could theoretically shrink the size considerably and increase the bandwidth of a patch antenna [24]. The miniaturization through magneto-dielectric utilization has been experimentally verified for a planar vivaldi antenna and a microstrip patch antenna [25], [26]. In [25], they discussed the harmonic distortion as well, but the lossy behaviour of the ferromagnetic material effectively behaves as a low pass filter preventing any meaningful harmonic distortion analysis.

Recent advancement in material science has led to the creation of Rogers Inc. MAGTREX 555 that incorporates a magneto-dielectric substrate to create a high wave impedance as described in [24], but with relatively low losses through the band of operation. Due to the relatively recent inclusion of these materials on the market, low-loss, high impedance magneto-dielectric substrates have yet to be investigated under stress. Therefore, Chapter 5 sets out to experimentally verify the application of a commercial grade, low loss and high impedance magneto-dielectric substrate for use with a broadband, miniaturized patch antenna and quantify the capabilities and limitations of such a material.

Chapter 2

Simulation Methods

In the earlier years of electrical engineering before computers were commonplace, analysis was often accomplished with closed expressions or calculations manageable on paper. This strategy offered great insight into the behavior of the systems under study and useful design equations. With modern computational power, however, design processes have been refined using simulation software. If the non-LTI analysis is to become widespread then there must be a commercial, off-the-shelf (CoTS) option. At the time of this writing Remcom's Xfdtd is the best option available for CoTS FDTD simulation software and is compared to SPICE models and another full-wave solver, High-Frequency Simulation Software (HFSS), to ensure its reliability. This investigation will also come with a brief overview of FDTD itself, and a comparison to a couple of other methods available.

2.1 Finite-Difference Time Domain

The Finite Difference Time Domain was originally theorized by Kane Yee in 1966 [27]. The purpose of developing the technique was there was not a generalized solution for time-dependent Maxwell's equations. While his original paper covered perfect electric conductors (PEC), he mentioned that it can be extended to other boundaries as well. Of course, today FDTD can handle a myriad of exotic materials and boundaries.

The numerical method uses the Central Difference derivative approximation to evaluate Faraday and Ampere's law, such that,

$$\frac{df(x)}{dx} \approx \frac{f(x+\frac{\Delta\ell}{2}) - f(x-\frac{\Delta\ell}{2})}{\Delta\ell} + O(\Delta\ell^2). \tag{2.1}$$

The error term for the method is $O(\Delta\ell^2)$, and will decrease or increase by a factor of $\Delta\ell^2$, so keeping the step size small is paramount to the accuracy of this method. Across $\Delta\ell$ the solution is assumed constant, meaning for an entire step in time, Δt, or in space, $\Delta\ell$, the fields will be assumed to be constant. To establish the numerical solution, Faraday's law is evaluated with central differencing, then solved for the H-field, and Ampere's law is evaluated and solved for the electric field in the same way.

The central difference approximation will only calculate between two points in its traditional state. Therefore, in order to move through space, Yee developed the Yee Grid. The Yee grid is a meshing of the simulation space on which Maxwell's equations are updated. The grid is two meshes, one magnetic and one electric offset from one another, where values are constant across any given cell between two calculated points. The H-fields and E-fields are calculated on their respective vertices of their grid, one at a time - where the E-field requires the H-field and vice-versa. As in (2.1), the two input points need to be staggered on either side of the output point. The staggering of the meshes allows the central difference approximation to take two offset points from one field quantity and calculate the value for the other field quantity as illustrated in Figure 2.1.

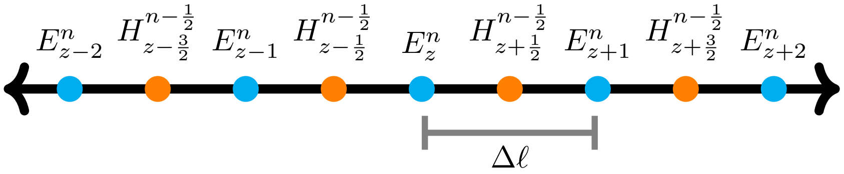

Figure 2.1: A representation of a small section of a Yee grid for a one dimensional FDTD simulation, where that dimension is the z-direction.

To move through time, the Yee grid is continuously updated as in Figure 2.2. The electric field is first calculated from some initial conditions, most commonly a voltage source of some kind, and both the E-field and H-field are left as 0 everywhere else. Then by calculating the electric field on that first step the algorithm has stepped forward in time. Next, the magnetic field is calculated, and this would progress the algorithm forward by half a time step as the act of physically calculating the magnetic field later in the code must denote some time passing. Going back to calculate the electric field from that magnetic field and any sources would complete one full-time step. Of course, this can be continued as long as necessary. The two most practical ways to determine termination are awaiting a steady-state or for all power to dissipate. Either case can be achieved within tolerance, as the first case may never be truly achieved due to numerical approximation and the second due to an impractical amount of time needed.

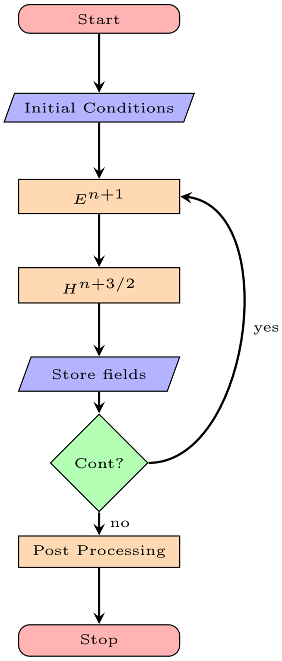

Figure 2.2: Rudimentary implementation of FDTD algorithm.

It is important to note that special care must be taken in the post-processing analysis since the E-fields and H-fields do not exist at the same locations. If only one quantity is used in a calculation, either electric or magnetic, then only locations that lie on that portion of the grid are achievable. This is especially important if the magnetic field on the surface of a conductor is desired, as the electric field was most likely calculated there and not the magnetic field. An easy solution is to take the cell average on either side of the point and use that as an approximation of the grid at the desired location. This is also problematic for port parameters, as both voltage and current may be needed, and both cannot exist right on the port simultaneously. There are different ways to solve this, simply taking the average is also acceptable here. While there are several other instances where the Yee grid's leapfrogging can be difficult in post-processing, there are plenty of solutions that are plenty accurate [11], [12] As mentioned previously, the update equations themselves come from Ampere's and Faraday's law,

$$\frac{\partial \boldsymbol{D}}{\partial t} = \nabla \times \boldsymbol{H} - \boldsymbol{J} \tag{2.2a}$$

$$\frac{\partial \boldsymbol{B}}{\partial t} = -\nabla \times \boldsymbol{E} - \boldsymbol{M}. \tag{2.2b}$$

Since there is plenty of well written educational material on FDTD the full derivation is not included here. To better understand the derivation, further reading [12] and [11] help immensely. For completion, the update equations for simple, lossy material with homogeneous grid spacing in one dimension are

$$H_y\Big|_i^{n+\frac{1}{2}} = \left(\frac{1 - \frac{\sigma_i^* \Delta t}{2\mu_i}}{1 + \frac{\sigma_i^* \Delta t}{2\mu_i}}\right) H_y\Big|_i^{n-\frac{1}{2}} + \left(\frac{\frac{\Delta t}{\mu_i \Delta x}}{1 + \frac{\sigma_i^* \Delta t}{2\mu_i}}\right) \left(E_z\Big|_i^n - E_z\Big|_{i-1}^n\right). \tag{2.3a}$$

$$E_z\Big|_i^{n+1} = \left(\frac{1 - \frac{\sigma_i \Delta t}{2\epsilon_i}}{1 + \frac{\sigma_i \Delta t}{2\epsilon_i}}\right) E_z\Big|_i^{n} + \left(\frac{\frac{\Delta t}{\epsilon_i \Delta x}}{1 + \frac{\sigma_i \Delta t}{2\epsilon_i}}\right) \left(H_y\Big|_i^{n+\frac{1}{2}} - H_y\Big|_{i-1}^{n+\frac{1}{2}}\right). \tag{2.3b}$$

2.2 Error and Stability of FDTD Algorithm

To understand the utility of any numerical method it is important to understand how accurate it is. Therefore, it would benefit to review the error analysis for the traditional, fully explicit FDTD method. The inherent error of the Central Difference Method is $O(\Delta\ell^2)$, and the error of this method will propagate throughout the simulation space. To limit this error, the temporal and spatial steps must be sufficiently small relative to the wavelengths of consideration. Often a max cell size of $\frac{\lambda}{10}$ is used [12]. While the entire algorithm's accuracy is more complex than just the error propagated by the derivative approximation, this second-order error term will govern the phase error and local convergence. Another consideration for accuracy is whether or not the simulation stays stable.

As much as it might be beneficial, FDTD is not unconditionally stable in its classical iteration, and some simulations may become unstable and tend towards $\pm\infty$. It is important to note that there is an unconditionally stable version that utilizes the alternating direction iteration method, but is not as widely used as avoiding instability in FDTD is not as difficult with modern computational power and affords little change in accuracy [28]. The Courant-Friedrichs-Lewy (CFL) stability limit is the limitation on the spatial and temporal steps to maintain a stable simulation [11], [12]. The CFL-limit is

$$\Delta t < \frac{1}{v_{\text{p max}}\sqrt{\frac{1}{\Delta\ell^2} + \frac{1}{\Delta y^2} + \frac{1}{\Delta z^2}}}, \tag{2.4}$$

where Δt is the temporal step, $\Delta\ell$, Δy, and Δz are the spacial steps, and $v_{\text{p max}}$ is the maximum phase velocity and is included in the case that the grid is non-homogeneous. The CFL limit is usually maintained by choosing the temporal or spatial step, and then set the other by a constant of proportionality. This is traditionally done with

$$\Delta t = \frac{\text{CFLN}}{v_{\text{p max}}\sqrt{\frac{1}{\Delta\ell^2} + \frac{1}{\Delta y^2} + \frac{1}{\Delta z^2}}}, \tag{2.5}$$

where CLFN is the CFL number and is usually set to 0.99. With both stability and local convergence quantified, by the Lax Equivalence theorem global convergence can be enforced [11]. It is important to keep in mind that the stability criteria are a significant limitation on simulation construction. To construct an incredibly fine spatial mesh the temporal step will need to be increasingly finer. This means the simulation will need to be run longer to allow a steady state to be reached or for enough of the power to dissipate from the simulation. This also restricts the size of the simulation space based on how fine of a mesh is desired, as that will result in an even longer simulation run time. There are, of course, methods to circumvent this, like using an unconditionally stable method or using anisotropic Yee-grids [28].

Global convergence is the standard goal for accurate numerical methods, however there is another error inherent the modeling method the Yee created known as numerical dispersion. Numerical dispersion is the error in wave propagation through some medium wherein the media is simulated as more dispersive than it should be. Numerical dispersion is measured by the comparing the exact wave number against the discrete wavenumber of the simulation, using the equation

$$\text{phase error}\left(\frac{\text{degrees}}{\lambda}\right) = \frac{180^o}{\pi}\left(\tilde{k} - k\right), \tag{2.6}$$

where the error in phase is measured in degrees per wavelength, $\tilde{k}$ is the discrete wave number, and k is the exact wave number. The exact wave number can be found in the usual way with $k = \frac{\omega}{v_p}$ and the discrete wave number is found for any particular time step using the Newton-Raphson's method for the function

$$f(\tilde{k}) = \frac{1}{c^2}S_t^2 - S_x^2 + S_y^2 + S_z^2, \tag{2.7}$$

where $S_t = \frac{1}{\Delta t}\text{sin}\left(\frac{\omega\Delta t}{2}\right)$, $S_\alpha = \frac{1}{\Delta\alpha}\text{sin}\left(\frac{\tilde{k}_\alpha\Delta\alpha}{2}\right)$, and $\alpha = x$, y, or z. Sampling the phase error is traditionally done with purely real wave numbers, if the wave number is complex that means the simulation resulted in a phase velocity faster than the speed of light, which for the antenna engineer should not be an issue that arises [11].

2.3 Sources of Error of Full Simulation Implementation

Despite minimizing the previously mentioned error and ensuring stability, there can still be sources of error, including poor meshing choices, added methods, ABCs, and post-processing. While the structure could be designed well, the mesh could be created incorrectly. Non-rectangular geometries, small gaps between materials, or structures far smaller than a practical Yee grid are common issues. Small gaps, like those found in substrate RF circuits, are difficult for the traditional Yee grid, even with a fully non-homogenous Yee grid [28]. This examination will coincide with the tests of Xfdtd as well, and all FDTD data from this point onward is a result of that software.

Conformal meshing allows FDTD to use a non-rectangular grid and exactly mesh to a surface. This does require the temporal step to be decreased sufficiently to meet the new spatial steps, as governed by the CFL-limit. Additionally, conformal meshing can better capture smaller gaps and any structure far smaller than the traditional spatial step [11], [12].

Singularity correction helps with increasing the confidence of boundaries, especially when the boundary is part of a small gap. Singularity correction can come in two forms. The simple method involves aggressively meshing at conductive or dielectric boundaries. Another method is to understand the modal behavior of a boundary and calculate the Electric field from that than directly from Maxwell's equations [29]. All three of these methods of improving the mesh on a structure are used in this thesis and are recommended for any complex structure.

These techniques' effectiveness is demonstrated in Figure 2.3. Additionally, these figures serve as a comparison to the effectiveness of Xfdtd as an antenna simulation software in comparison to HFSS. The imaginary input impedance between

FDTD and HFSS are very close, while the real impedance is off by about 4% at the operating frequency between one another. The S_{11} of each simulation is very close to the location of the most power transferred to the antenna. The difference in minimas of S_{11} correlates to the slight difference in real impedances, where the FDTD simulation is 2 Ω closer to the system impedance of the antenna ports.

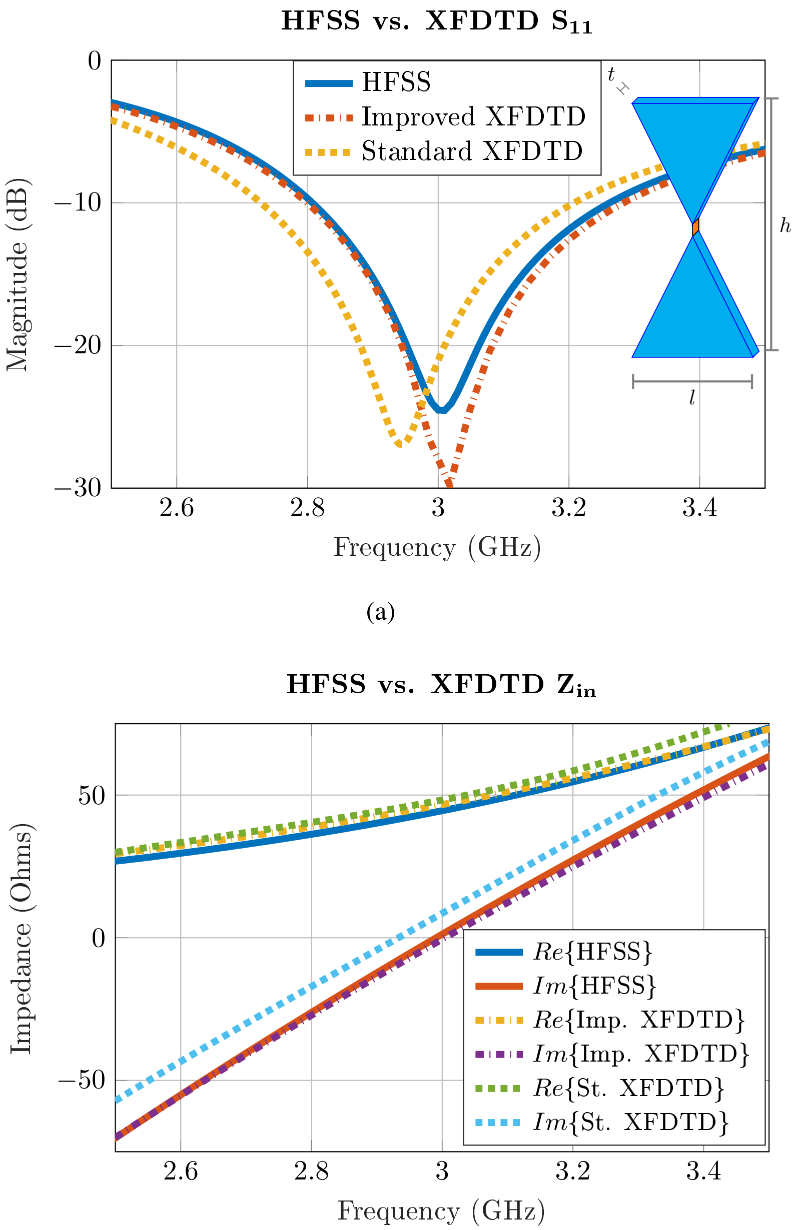

(a)

(b)

Figure 2.3: Bowtie dipole designed for 3 GHz, where l = 7.79 mm, h = 36.29 mm, and t = 0.3 mm

Lumped Components are a vital inclusion in to FDTD simulation, but are not without some errors. Resistive Loads are the most accurate of the lumped components available as they exist with a simple I-V relationship. Comparing an FDTD

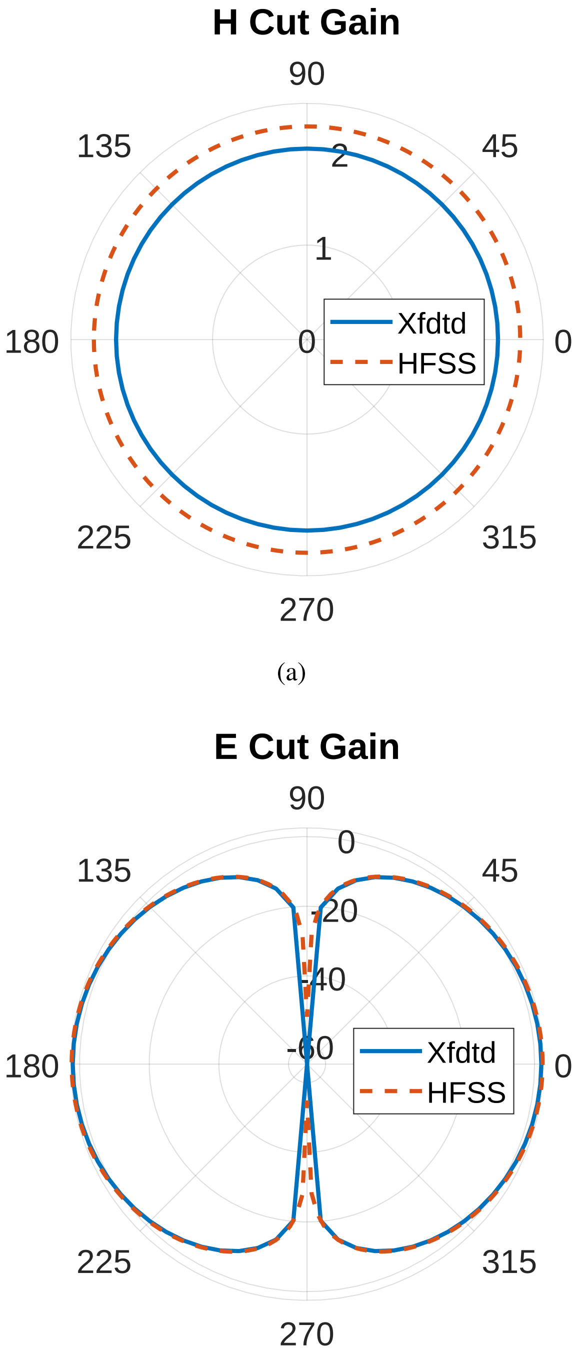

(a)

(b)

Figure 2.4: Gain of the Bowtie antenna from 2.3

implementation with a common SPICE modeler, as shown in Figure 2.5 reiterates this point. RLC models are accurate enough as well, but with some slight errors as shown in Figures 2.7 and 2.8.

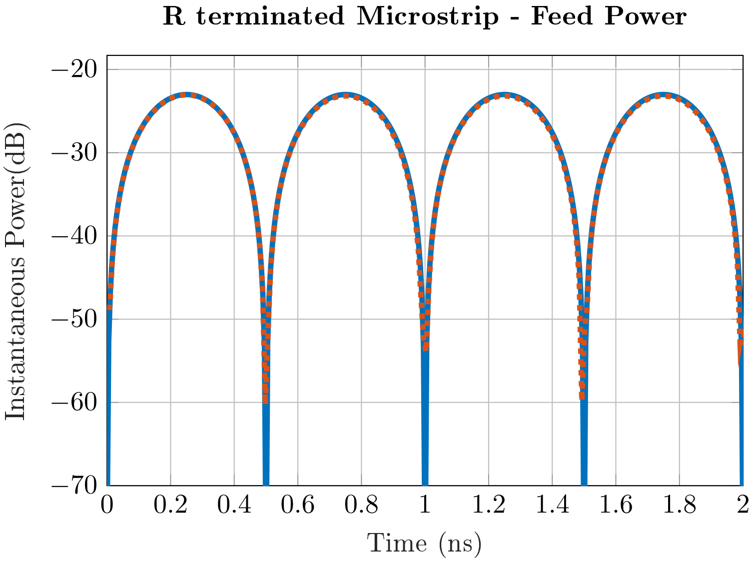

(a) 1 V, 50 Ω input

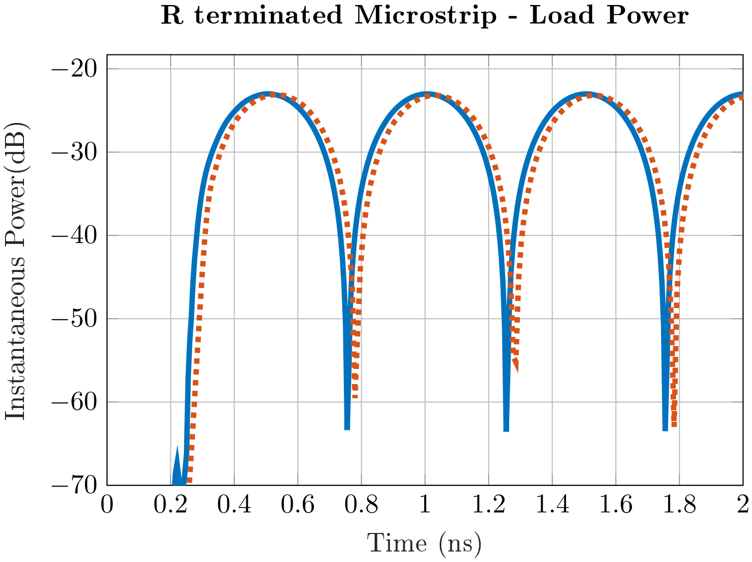

(b) 50 Ω load

Figure 2.5: Microstrip transmission line terminated with a matched load.

Moreover, a real-valued load with a high reflect also sees some slight disagreement. Because the Yee grid offsets the H-field quantity, many post-processing calculations require some approximation [12]. Not only does the high reflection load experience this, but this approximation must affect the RLC loads as well.

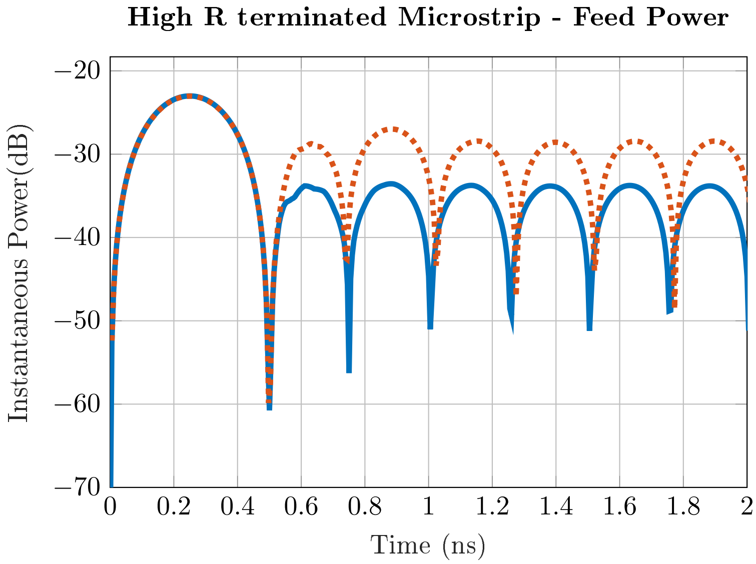

(a) 1 V input, 50 Ω input

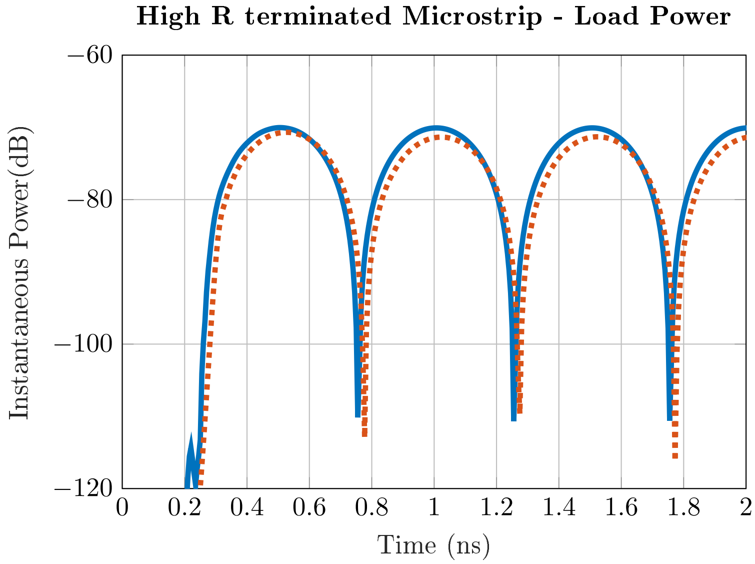

(b) 10 MΩ load

Figure 2.6: Microstrip transmission line terminated with a large resistance.

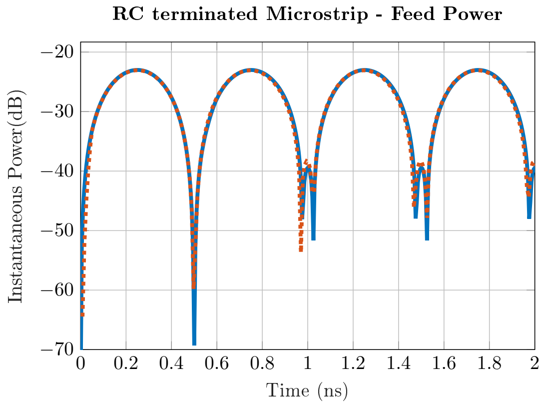
RC terminated Microstrip - Feed Power

(a) Shunt RC with R = 50 Ω, C = 1 pF

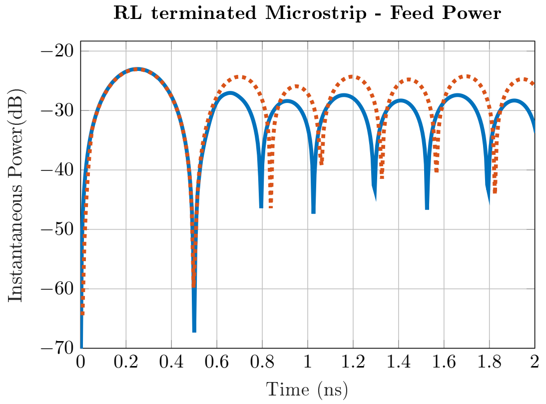
RL terminated Microstrip - Feed Power

(b) Shunt RL with R = 50 Ω, L = 1 nH

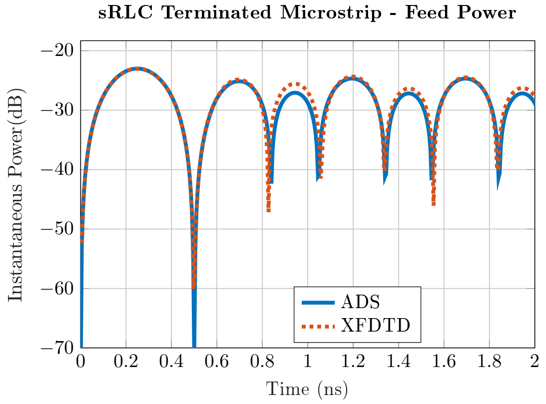
sRLC Terminated Microstrip - Feed Power

(c) Shunt RC with R = 50 Ω, C = 1 pF, L = 1 nH

Figure 2.7: Microstrip transmission line terminated with a shunt RC, a shunt RL, and a series RLC tank. Data here is from the feed on the line, with a 1 V input, 50 Ω input.

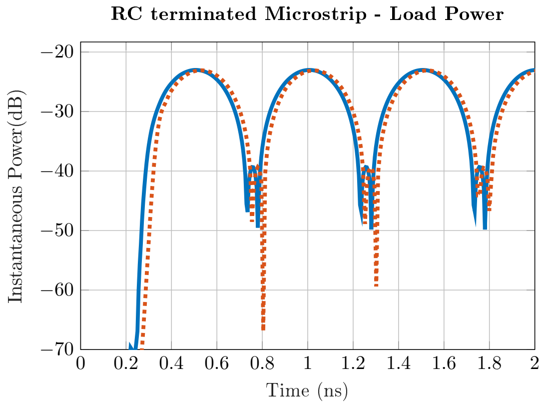

(a) Shunt RC with R = 50 Ω, C = 1 pF

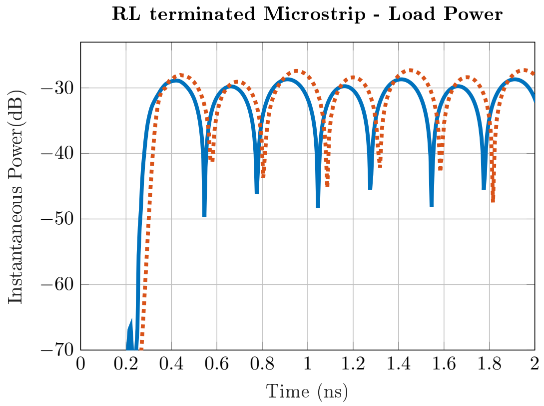

(b) Shunt RL with R = 50 Ω, L = 1 nH

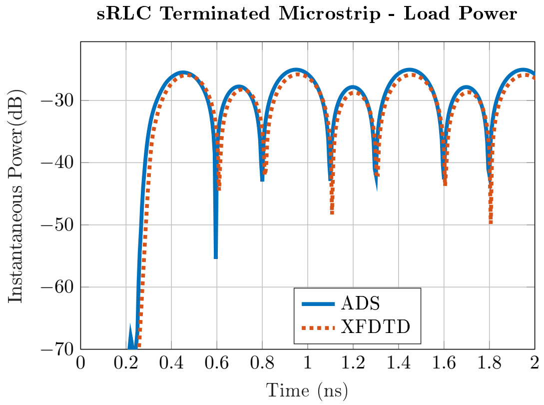

(c) Shunt RC with R = 50 Ω, C = 1 pF, L = 1 nH

Figure 2.8: Microstrip transmission line terminated with a shunt RC, a shunt RL, and a series RLC tank. Data here is from the load on the line.

Another source of error can come from the Absorbing Boundary Condition (ABC) used. Perhaps the most accurate and robust method is the Complex, Frequency Shifted Perfectly Matched Layer (CFS-PML) [12]. The PML used in FDTD was originally formulated in [30] and is quite accurate for a general simulation down to a particular frequency. The CFS-PML improves upon that and removes the stability condition. By considering the complex plane of the transfer function of the PML, the point at which instability occurs will be represented as a pole. By using a particular tensor coefficient, the pole is shifted into the negative side of the frequency spectrum. This makes the PML stable for arbitrarily low-frequency values, as the FDTD method will never simulate a negative frequency since it is a time-domain method [31]. The error experienced by the CFS-PML is quantified by the chosen coefficients and is detailed in [12]. Since the results in Figure 2.4 are satisfactory, it can be concluded that Xfdtd correctly implemented their boundary conditions, and as there is no limit on the run-time of the simulations, it can be assumed a CFS-PML was implemented.

The last major element worth validating is the non-LTI capabilities of FDTD. Time-varying elements are perhaps the simplest to incorporate, as their inclusion is native to the FDTD method. An example is a switch or other time-varying conductivity. To implement a distributed time-varying conductivity, the mesh on which the FDTD algorithm takes place merely needs to be updated at appropriate time steps and locations. A PEC switch is the simplest of these examples. To incorporate it the algorithm needs to set the electric field at the location of the switch to 0 when it is closed, and then allow the electric field to pass when it is opened. This is most efficiently done by having a vector of coefficients to correspond to the open and close states, where open is a 1 and closed is a 0. Figure 2.9 demonstrates the reliability of Xfdtd's switch with a time-varying bowtie antenna. This example uses a bowtie antenna with an incident wave at 3 GHz, and a switch across the feed of the antenna opening and closing rapidly at 10 MHz, where $\ell = 36$mm and $\alpha = 155^o$.

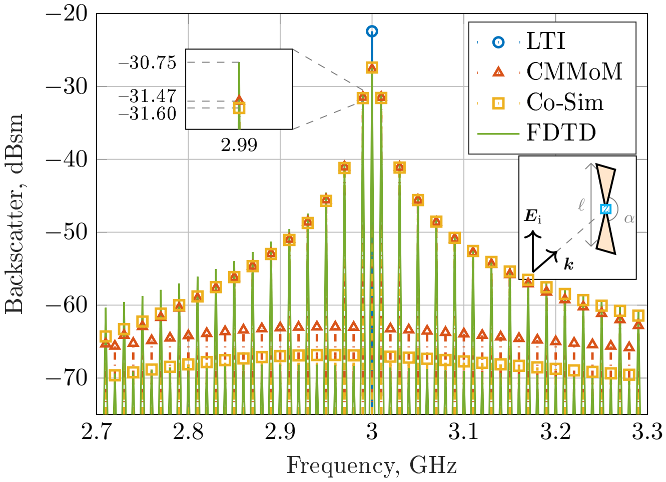

Figure 2.9: Xfdtd comparison to multiple time-varying simulation methods [15].

Nonlinear elements are not nearly as simple to implement, as they require some form of cosimulation or fundamental alteration to the algorithm. Here, cosimulation will be understood as the act of pausing one numerical method to begin another one, that is a constituent of the first method, and whose results will be inserted back into the first to continue the simulation at large. An example would be the use of SPICE in a full-wave solver, where the full-wave solver pauses itself when it arrives at the location of the lumped element modeled by SPICE, runs the SPICE analysis using inputs from the full-wave solver, then uses the results of the SPICE simulation to continue on the full-wave solver in place of just solving another grid point or face where the SPICE element was. For this final evaluation, the diode implementation was investigated, and the most common implementation is,

$$
\begin{aligned}
E_{\hat{\mathrm{a}}}\Big|^{n+1}_{(\mathrm{i,j,k})} = E^{n}_{\hat{\mathrm{a}}}\Big|^{n}_{(\mathrm{i,j,k})} + \frac{\Delta t}{\epsilon_0}\left(\nabla \times \mathbf{H}\right)_{\hat{\mathrm{a}}}\Big|^{n+\frac{1}{2}}_{(\mathrm{i,j,k})} \\
- \frac{I_s \Delta t}{\epsilon_0 \Delta\ell \Delta y}\left\{ \exp\left(\left(E_{\hat{\mathrm{a}}}\Big|^{n+1}_{(\mathrm{i,j,k})} + E_{\hat{\mathrm{a}}}\Big|^{n}_{(\mathrm{i,j,k})} \right) \frac{\Delta z}{2V_{\mathrm{T}}} \right) - 1 \right\}, \quad (2.8)
\end{aligned}
$$

and can be found in [11]. This method is an improvement on the original, as it is stable up to 15V thanks to its implicit form - it is dependent on the current and the next time step. Unfortunately, comparing this to the Xfdtd implementation,

$$
I_D = I_s \left(\exp \frac{V}{nV_{\mathrm{T}}}) - 1 \right), \quad (2.9)
$$

Remcom implemented a more unstable version of the diode as the V here is dependent only on the current time-step and not the current and next. Attempts at getting the diode algorithm to operate stably under normal parameters proved to be nearly impossible. Figure 2.10 shows the results of a simulation using the bowtie dipole from 2.3, where the feed has a diode across it. The explicit form of the diode is only stable to 0.8 V, and Figure 2.3 shows that shortly before one volt, the current across the diode becomes unstable and tends towards infinity [11]. This occurs with the parameters I_S=1e-12A, $\mathrm{V_J}$, $\mathrm{C_D}$=0.3 pF, τ=0.001 ns, and grading, emission, and forward coefficients set to 1. It can be concluded, then, that a reasonable antenna simulation including a diode is not a simulation Xfdtd can handle well.

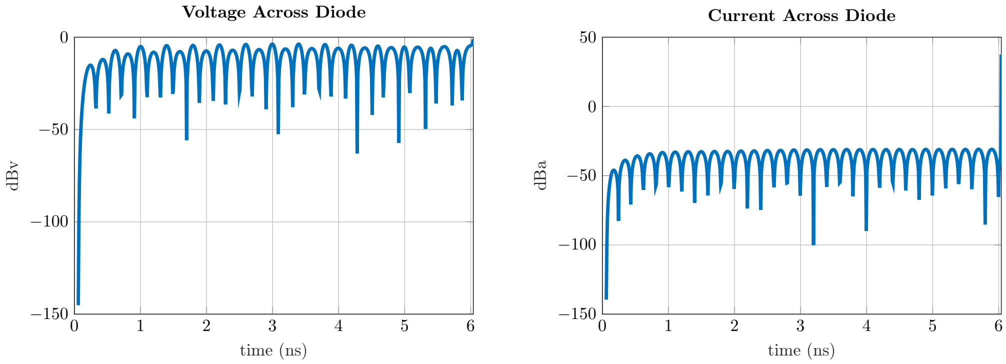

Figure 2.10: V and I across the diode.

2.4 Alternatives

While the following alternatives do not have CoTS versions, their relatively simple implementation and marriage with CoTS CAD software make them extremely versatile. These alternatives are included to better understand the environment of non-LTI simulation methods. It is also useful to have a few methods to choose from, as it is important to corroborate simulation data for accuracy and each method has its strengths and weaknesses.

2.4.1 Conversion Matrices

The first, Conversion Matrices (CM), revolves around the usage of N-port networks being used to represent Ohm's law in a time-varying element in the frequency domain [14], [32]. The primary difference between a normal N-port is that each port represents a particular harmonic, such that the feed location on an antenna may have several ports correlating to all the harmonics under consideration in the particular simulation. The conversion matrix itself looks much like a reciprocal N-port network matrix, except it represents only one physical port. Ohm's law in the frequency domain when the impedance is time-varying results in a frequency domain convolution. This impedance is modeled using a Fourier series, as are the voltage and currents in the convolution as well. This results in Ohm's law being represented with

$$\begin{bmatrix} V_{-M} \\ V_{1-M} \\ \vdots \\ V_{M} \end{bmatrix} = \begin{bmatrix} Z_0 & Z_{-1} & \cdots & Z_{-2M} \\ Z_1 & Z_0 & \cdots & Z_{1-2M} \\ \vdots & \vdots & \ddots & \vdots \\ Z_{2M} & Z_{2M-1} & \cdots & Z_0 \end{bmatrix} \begin{bmatrix} I_{-M} \\ I_{1-M} \\ \vdots \\ I_{M} \end{bmatrix}, \tag{2.10}$$

where M is some integer number, and the subscripts denote what harmonic each Fourier coefficient corresponds to. M must be sufficiently large enough to consider every sufficiently large harmonic component and ideally is infinitely large. However, truncating out to a realizable number is necessary for calculation and often a safe assumption.

Therefore, to enact a CM simulation, one simply needs the Fourier series coefficients of either voltage or current, and the impedance of the element under consideration. To use this with a full-wave solver, a method of moments (MoM) impedance matrix can be used in conjunction, where an arbitrary number of locations in the matrix can be loaded with conversion matrices for an accurate and efficiency time-varying solution method [15].

2.4.2 Harmonic Balance

Harmonic balance (HB) is another method that takes an N-port representation, but this time uses it to segregate the linear and nonlinear portions of a simulation [14], [32]. There are a minimum of two subcircuits, where one is linear and the other is nonlinear. The linear portion is solved with the nonlinear portion disconnected, and the resulting voltage and currents on the port to the nonlinear section. Then one of those values is used as the input to the nonlinear section, and the nonlinear section is solved. Then, the value that was not used to solve the nonlinear portion is compared between what the linear and nonlinear subcircuits arrived at. In a standard, linear system these values would be equal. However, with the nonlinear circuit, this is not necessarily true, and the difference between these two values represents the error term in the solution. Then using any root finding or optimization method desired, the error term can be minimized and a sufficiently accurate solution can be arrived at. Just like with CM, MoM can be used in conjunction with an HB simulation on an arbitrary number of ports to represent any nonlinear system provided a proper numerical representation exists.

2.5 Concluding Remarks

For non-LTI analysis to become commonplace, it is necessary to have robust and reliable simulation methods. Without such, non-LTI designs will be far too cumbersome for widespread adoption. There do exist a few other FDTD commercial software, like Ansys Lumerical or FEKO's FDTD solver, but as these companies did not prioritize their non-LTI packages they do not satisfy the need for a true non-LTI full-wave solver. It then falls to Xfdtd to fulfill this need, and in some instances, it performs well. It is a satisfactory alternative to HFSS and does a good job of running switching simulations. However, its nonlinear aspects are left wanting. At the time of this writing, they have recently released a version that includes a SPICE co-simulation option and maybe the solution to handling more complex non-LTI problems. Therefore, Xfdtd cannot be entirely ruled out as a possible choice for CoTS non-LTI simulation software.

The alternative is to write code that handles the simulation. FDTD is a front runner as it can handle a plethora of non-LTI problems an antenna engineer would consider. However, there are also CMMoM and HBMoM that can leverage CoTS MoM solvers, like FEKO, to generate complex geometries that make coding more surmountable when antennas are more complicated than simple wires and planes are being studied. However, they come with the drawback of not being nearly as well documented, and non-LTI components exist as lumped components. Although, these lumped networks can be used to approximate distributed elements or behavior by being applied to a large number of the MoM ports. In conclusion, while computational electromagnetics has come a far way, it may still be necessary to code individual simulations in-house for non-LTI designs.

This chapter focused on how the design process may take place in a non-LTI system. In the next chapter, analysis techniques for such systems will continue. However, the next chapter will focus on reactive power in nonlinear systems. More specifically, how reactive power is defined in nonsinusoidal systems, if a better way to characterize it exists, and if it can be useful.

Chapter 3

Reactive Power and Harmonic Power-Balance Relations

> If all electrical iron could by divine decree or presidential proclamation be straightened into uniform permeability over its whole range of magnetization there would be less occasion to raise the question of adequacy of our prevailing concepts of reactive power and power factor. If all synchronous machine windings under all conditions of loading could have flux distribution in strict conformity with symmetrical sinusoidal generation there would be still less. Moreover, the excuse would nearly vanish if polyphase circuits could always be held to rigid balance of impedances on their lines and loads. With these factors eliminated the residue of doubt, if any, would be a topic to intrigue only the academic and metaphysical minds [33].

3.1 Motivation

It had been posited in [32] that utilizing a time-varying resistor in an antenna could cancel out the antennas reactance and result in a novel matching technique. It was mentioned in [18] that a time-varying resistor generators reactive power, so this concept showed some promise. While there were some results in [32] that leveraged optimization methods to show that low frequency, ultra-broadband matching may be possible, the losses in the resistor in most cases made the concept very inefficient. While these results were arrived at largely through simulation and CM analysis, it was of interest to take a more generalized approach to try and understand reactive power in a time-varying resistor. The derivation in this thesis attempts that, and includes an analysis of reactive power in the non-sinusoidal case - a result of nonlinear systems. This chapter will demonstrate the fruitlessness of attempting to incorporate reactive power of nonlinear system into novel RF solutions.

3.2 Introduction

Reactive power has been historically ill-defined in non-LTI systems. Both the physical understanding and mathematical representation of reactive power stemmed from its behaviour in an LTI system. In that instance, the orthogonal component to the real power that oscillates between the source and a load is a complete and useful definition - and the one most engineers are familiar with [34]. The physical manifestation of the nonactive power in a non-LTI system, on the other hand, is not clearly defined in a physical system [35], [36]. When handling nonactive power, the current calculation method is to merely define a ratio to quantify how much of a signal was lost to harmonic distortion [34]. This method has proven to be useful in characterization for the purpose of comparing and contrasting systems, but fails to do much more. Measuring distortion power, the nonactive power that arises from nonlinearites, is also an arduous task that is not done as simply as most other electrical measurements, like voltage, current, resistance, and real power [36].

A foundational relationship for understanding real power in a polyharmonic system is the Manley-Rowe (MR) power balance relations [18]. These expressions concisely describe the interplay of harmonic power within a nonlinear reactance, and are the basis for parametric amplification. They went on to derive similar power balance relations for a nonlinear resistor, but unfortunately were useless compared to the relations for a nonlinear reactance.

By their own admission, the MR reactive power relations and analysis were no good. The original reactive power relation was just an exact re-application of the active power derivation, but instead applied to a real-valued time-varying load instead of a complex-valued one. According to Manley and Rowe, these relations did not explain anything useful, being nothing more than a restricted weighted sum of forms,

$$\sum_{\ell=-\infty}^{\infty}\sum_{k=0}^{\infty} k N_{k,\ell} = 0 \tag{3.1a}$$

$$\sum_{\ell=-\infty}^{\infty}\sum_{k=0}^{\infty} \ell N_{k,\ell} = 0. \tag{3.1b}$$

Surprisingly, Manley and Rowe also noted that reactive power is not conserved in a nonlinear resistor, and base it off analysis done with these two relationships. The verification of this statement today is more difficult as the definition used by Manley and Rowe is no longer accepted. In order to verify this statement and understand the limitations of analyzing reactive power in a nonlinear system, reactive power conservation under the current definitions is investigated and more useful expressions are derived.

3.3 Reactive Power Investigation

The following is a summary of the mathematical principles of reactive power in the original Budeanu definition and in the current one as stated in the IEEE definition. This selection is predicated on the fact that the Budeanu definition was widely used in the 1900's as a modified version was accepted by the AIEE. Therefore, older literature is most likely operating under this definition. Of course, the IEEE definition overtook that one and is commonly seen in this century.

3.3.1 Sinusoidal

Two dimensional power is a concept that works well for sinusoidal conditions. One dimension describes the power that flows from one element to another, know as the instantaneous active power, that can be described with,

$$p_a = VIcos(\theta)[1 - cos(2\omega T)] = P[1 - cos(2\omega T)], \tag{3.2}$$

where V and I refer to the rms values of voltage and current, and θ the angle between them. For the duration of this section capital letters refer to the RMS values. Then there is the power that flows between the two, known as the instantaneous reactive power, and can be described similarly to (3.2) as,

$$p_q = -VI\sin\theta\sin(2\omega T) = -Q\sin(2\omega \mathrm{t}). \tag{3.3}$$

This leads to the vector formed by these two orthogonal components, the apparent power, which describes that maximum active power delivered to an element as

$$S = VI = \sqrt{P^2 + Q^2}. \tag{3.4}$$

3.3.2 Nonsinusoidal

Budeanu Definition

For a non-sinusoidal case where harmonics are considered this definition becomes insufficient, and a three dimensional case is instead considered where apparent power is the vector comprised of the orthogonal versors formed by active power, reactive power, and distortion power - a new quanitity included as just reactive power is no longer the only nonactive power present [19], [33]–[37]. This vector apparent power is defined similarly to the sinusoidal case as,

$$S = \sqrt{P^2 + Q^2 + D^2} = VI = \sqrt{\sum_h^H V_h^2 \sum_h^H I_h^2}, \tag{3.5}$$

and the three components are defined as,

$$P = \sum_h^H V_h I_h \cos(\theta_h) \tag{3.6a}$$

$$Q = \sum_h^H V_h I_h \sin(\theta_h) \tag{3.6b}$$

$$D = \sqrt{S^2 - P^2 - Q^2}, \tag{3.6c}$$

where D is the distortion power. In order to give a real definition to distortion power aside from simply being the portion left over from the other two dimensions, Budeanu used Lagrange's identity,

$$\sum_{h=1}^H A_H^2 \sum_{h=1}^H B_h^2 - \left(\sum_{h=1}^H A_h B_h \right)^2 = \sum_{m=1}^{H-1} \sum_{n=m+1}^H (A_m B_n - A_n B_m)^2 \tag{3.7a}$$

$$|\overline{A}|^2 |\overline{B}|^2 - (\overline{A} \cdot \overline{B})^2 = |\overline{A} \times \overline{B}|^2, \tag{3.7b}$$

with the definition for distortion power in (3.6) to arrive at

$$D = \sqrt{\sum_{m=1}^{v-1} \sum_{n=m+1}^{v} [(V_m I_n)^2 + (V_n I_m)^2 - 2V_m V_n I_m I_n cos(\theta_m - \theta_n)]}. \quad (3.8)$$

This showed that to calculate the distortion power, one only needed to calculate $D = |\overline{V} \times \overline{I}|$, or the cross products of different harmonic voltages and currents. This definition, which had been arrived at completely mathematically, implies that the existence of inter-harmonic effects generated the distortion. Some lambasted this definition on the grounds it had little physical meaning and failed in some situations [36]–[39]. One particular issue centered around the inability to condition power in the presence of intermodulation distortion, as even a simple tuning shunt capacitor selected to cancel out Q would leave the distortion power intact if at least changed, and the power factor still undesirable [36]. It can be shown that even the simple act of rejecting Budeanu's distortion power as defined in (3.8) and interpreting a matching problem from an RF perspective will result in desirable effects - E.G. conjugate matching the impedance, not the power, in a polyharmonic system. While the distortion power may seem unintuitive in this state, the overall idea of distortion power brought on by nonsinusoidal conditions will remain throughout many definitions, including the current IEEE definition.

IEEE 1459-2010 Definition

In the IEEE Standard 1459-2010, reactive power was given a new definition that makes more physical sense and is more correct in all cases [37]. The predominant differences are that active and nonactive power are defined with fundamental and harmonic components, where the fundamental frequency powers are the same as the sinusoidal case, P and Q in (3.2) and (3.3), such that the nonsinusoidal case will simply collapse and agree with the sinusoidal definitions of power. The harmonic components are then defined as

$$P_H = V_0 I_0 + \sum_{h \neq 1} V_h I_h \cos(\theta_h) = P - P_1, \tag{3.9}$$

for active harmonic power where P_1 refers to the active power at the fundamental frequency and,

$$(\mathrm{THD_V}) = \frac{V_H}{V_1} \tag{3.10a}$$

$$(\mathrm{THD_I}) = \frac{I_H}{I_1}, \tag{3.10b}$$

define the total harmonic distortion for voltage, $(\mathrm{THD_V})$, and current, $(\mathrm{THD_I})$. The THD figures are the most interesting update to note, as they give a physical meaning to what distortion is in relation to the fundamental frequencies' power. For completeness, the final power figures are,

$$S_H = V_H I_H = S_1 (THD_I)(THD_V) = \sqrt{P_H^2 + D_H^2} \tag{3.11a}$$

$$S = \sqrt{S_1^2 + S_H^2} = (VI)^2 \tag{3.11b}$$

$$N = \sqrt{S^2 - P^2}, \tag{3.11c}$$

where N is the total nonactive power - known often as fictitious in earlier literature. The summary of the 1459-2010 will end here as their definitions suit a power engineer's needs far more than an RF engineer's. The important distinctions here are that no additions have been made to enforces conservation, and THD is the language in which nonactive power and harmonics are discussed.

3.4 Reactive Power Conservation

In Knowlton's summary of the 1933 A.I.E.E. proceedings on reactive power there are some observations that may raise questions for those outside of power engineering. In particular, the statement that reactive power is not conserved between circuits of differing frequencies [33]. The example mentioned is that between a stator and rotor of an induction motor. Knowlton is most likely referring to the model of an induction motor where the stator and rotor exist as a transformer, and in many cases will behave in a nonsinusoidal condition any time a steady-state is left. This line is not restricted to different circuits, however, as distortion power has been shown to simply not be conserved across frequency when the scalar definitions are used [39], [40]. Unfortunately, this is not the only issue with distortion power raised by the conference.

Another interesting consequence of the proceedings of that A.I.E.E. meeting was a few notions about what reactive power truly was. Most accept that reactive power is the portion of the power stored as an oscillation between the source and some load. If this is the case, then the mean value of this power is 0 and must be a wholly fictional quantity [33]. This is assuredly a point of debate since energy storage is often a meaningful phenomenon in high-frequency structures. That is perhaps a reason behind the definition of quality factor, as stored energy is of concern and not power. Another issue they brought to light was the electromagnetic definition of reactive power for a sinusoidal state,

$$Q = 2\omega(W_m - W_e), \tag{3.12}$$

and what ω truly meant in a nonsinusoidal case and if superposition would hold.

This extends to quality factor as it requires stored energy in its' definition.

The most troublesome realization was that harmonics of voltage or current would affect different harmonics of the other quantity, such that reactive power would not be a superposition of the power at each harmonic only, and distortion power would be all other nonactive power. The conference concluded, with some dissension, that reactive power should only consider the components at their respective frequencies as in (3.6) to avoid any of the aforementioned concerns.

This leads then to Manley and Rowe's claim that in the nonlinear resistor's reactive power will not be conserved and that reactive power is not well defined [18]. Manley and Rowe must be referring to the general notion of reactive power when the interhamronic effects have not to be allocated to distortion power. In this case, reactive power is a poorly defined physical quantity and cannot be conserved across frequency making design equations and principles difficult to formulate - especially since their relation to nonlinear resistors was not explanatory in its' own right. Additionally, if taken purely mathematically, they used a reactive power definition that most closely resembles (3.11c), where what they claim to be reactive is all power left over after active power has been removed from the apparent power. Thankfully, there are alternative understandings to reactive power that may benefit both a qualitative and quantitative analysis.

Alternate Forms

While the current IEEE definition is largely accepted and has much utility, it would help to look at a couple of alternatives that alleviate issues still present in the IEEE definition - as it avoids delving much further into a physical understanding or reconciling conservation. One good candidate is laid out in [41], as it makes physical sense, is correct mathematically in all cases, and is easily measured unlike most other forms of distortion and reactive power [33], [41]. The currents of a nonsinusoidal system are decomposed into three orthogonal components. However, this time they are delineated as the active current, reactive current, and scattered current and are defined as,

$$||i_a|| = \frac{P}{||v||^2} \tag{3.13a}$$

$$||i_s|| = \sqrt{\sum_{h \in H} (G_h - G_e)^2 V_h^2} \tag{3.13b}$$

$$||i_r|| = \sqrt{B_h^2 V_h^2} \tag{3.13c}$$

respectively, where G and B refer to the conductance and susceptance, G_e refers to the conductance at the excitation frequency, and H is the set of all harmonics. Under this definition, the active current refers to that which is transmitted and absorbed in a system, the scattered current is that which is transferred to other harmonics, and the reactive current is that which oscillates, or is stored, at each harmonic. Using these currents to calculate power gives clearly defined physical definitions for all three dimensions, and accounts for all power in a nonsinusoidal system.

Another alternative is that explained in [40] to correct the power conservation issue for periodic signals who contain distortion. While complex power is a three dimensional vector in the nonsinusoidal case, generally only scalar quantities are used for calculating power. Instead, [40] opts to calculate them from vector representations of current and voltage. The authors use the inner product and norm definitions

$$\langle x(t), y(t)\rangle = \frac{1}{T}\int_0^T x(t)y(t)\mathrm{d}t \tag{3.14a}$$

$$||x(t)|| = \langle x(t), x(t)\rangle. \tag{3.14b}$$

Then a conserved defintion of reactive power, along with the corresponding active and apparent powers, are,

$$S = ||V||||I|| \tag{3.15a}$$

$$P = V^{\mathrm{T}} I \tag{3.15b}$$

$$R = (VI^{\mathrm{T}} - IV^{\mathrm{T}}). \tag{3.15c}$$

These are but two options, and there are several other available.

3.5 Derivation

Now that there is a solid understanding of what reactive power is meant in this case, the derivation can begin. First, consider a voltage source at an excitation frequency ω_0 mixing with a resistive, time-varying load at a pumping frequency ω_1. The time-varying load can either be linear or nonlinear, but is assumed to have no hysteresis. The diagram in Figure 3.1 is a physical manifestation of the system across all harmonics. The circuit represents a nonlinear resistor, R_{NLTI}, in an idealized system where it will generate harmonics. Each generic component represents some ideal filtering occurring at ω_n, a reactance across which the reactive power will be stored, and a possible voltage source at any harmonic. For this derivation, the sources will be zero at all harmonics except ω_0 and ω_1. The inclusion of the three dots represents that this system continues on to consider all harmonics, which is theoretically an infinite number. However, it will normally be truncated to N number of harmonics in a realized system. The most important assumption is the existence of reactance at each harmonic, as they will be required to store power at any particular harmonic. The proceeding derivation will involve the nonlinear resistor, the reactance, V_0, $V_1 \neq 0$ and all other sources zero, and will not truncate the number of harmonics considered.

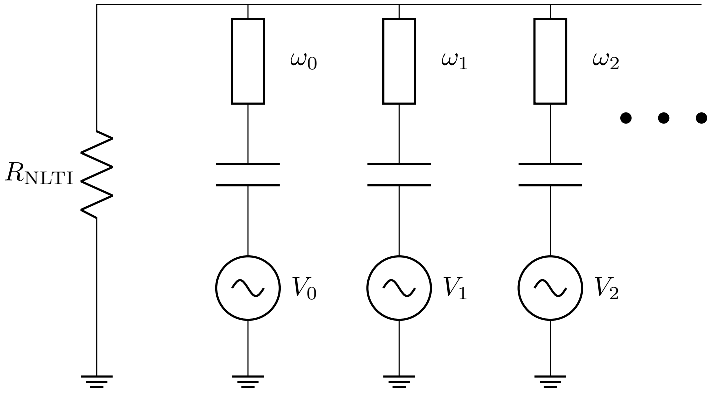

Figure 3.1: Circuital representation of the reactive power balance relation.

To examine the behavior of a nonlinear resistive element, it would make sense to use Fourier Series representations to inspect harmonics - so the Fourier Series representations of the voltage and charge along the resistive element will be utilized. To abstract the excitation and pumped sources, each will be assigned an independent time variable, t and t' respectively. A realized system will have some linear relationship between the two variables to reflect the possibility of different starting times for each source, such that $t' = at + b$. The rate of time passage between the two will still be equal, and we can assume for the derivation that they start at the same time. This is a needed assumption to carry out any two-dimensional vector operators, and the derivation will not lose generality. While this decision may seem cumbersome, it permits the usage of the crucial, two-dimensional Fourier Series representations of charge and voltage,

$$q(t,t') = \sum_{k=-\infty}^{\infty} \sum_{\ell=-\infty}^{\infty} Q_{k\ell} e^{j(\ell\omega_0 t + k\omega_1 t')} \tag{3.16a}$$

$$v(t,t') = \sum_{k=-\infty}^{\infty} \sum_{\ell=-\infty}^{\infty} V_{k\ell} e^{j(\ell\omega_0 t + k\omega_1 t')} \tag{3.16b}$$

$$Q_{k\ell} = \frac{\omega_0}{2\pi} \int_0^{2\pi/\omega_0} \frac{\omega_1}{2\pi} \int_0^{2\pi/\omega_1} q(t,t') e^{-j\ell\omega_0 t} e^{-jk\omega_1 t'} \mathrm{d}t\mathrm{d}t' \tag{3.16c}$$

$$V_{k\ell} = \frac{\omega_0}{2\pi} \int_0^{2\pi/\omega_0} \frac{\omega_1}{2\pi} \int_0^{2\pi/\omega_1} v(t,t') e^{-j\ell\omega_0 t} e^{-jk\omega_1 t'} \mathrm{d}t\mathrm{d}t', \tag{3.16d}$$

where ℓ and k refer to the harmonic indices of the excitation and pumped frequencies respectively. Next, we would like a relationship between charge and current in reference to both time variables, requiring the gradient of the scalar charge,

$$i(t) = \left(\frac{\partial}{\partial t} + \frac{\partial}{\partial t'} \right) q(t,t'). \tag{3.17}$$

Note that this is nothing more than the definition of current extended into two dimensions with an assumed linear relationship between t and t'. By using this relationship on the Fourier coefficient for charge and current the following is obtained,

$$\sum_{\ell=-1}^{1} \sum_{k=-\infty}^{\infty} I_{k\ell} \mathrm{e}^{j(\ell\omega_0 t + k\omega_1 t')} = \sum_{\ell=-1}^{1} \sum_{k=-\infty}^{\infty} j\left(\ell\omega_0 + ak\omega_1\right) Q_{k\ell} \mathrm{e}^{j(\ell\omega_0 t + k\omega_1 t')}, \tag{3.18}$$

and then matching frequency terms, a relationship between the current and charge Fourier coefficients can be written as,

$$I_{k\ell} = j(\ell\omega_0 + ak\omega_1)Q_{k\ell}, \tag{3.19}$$

whose conjugate will form the denominator of the power balance relationship. Additionally, we would like a relationship between the derivative of the current function and the charge Fourier coefficient such that

$$\frac{\partial i}{\partial t'} = \sum_{\ell=-\infty}^{\infty} \sum_{k=-\infty}^{\infty} Q_{k\ell}^{*} \mathrm{e}^{-j(\ell\omega_0 t + k\omega_1 t')}(-k^2\omega_1^2), \tag{3.20}$$

whose substitution in the next step will greatly simplify the final expression.

After multiplying both sides of the voltage Fourier coefficient expression in (3.16d) by $-Q_{k\ell}^{*}k^2\omega_1^2$ summing over all k and ℓ, substituting in (3.19) to the left side, (3.20) to the right, and applying the chain rule, (3.16d) becomes

$$\sum_{\ell=-\infty}^{\infty} \sum_{k=-\infty}^{\infty} \left(\frac{(-k^2\omega_1^2)V_{k\ell}I_{k\ell}^{*}}{j(\ell\omega_0 + k\omega_1)} \right) = \frac{\omega_1}{2\pi} \int_{i(0,t')}^{i(2\pi/\omega_1,t')} \frac{\omega_0}{2\pi} \int_{0}^{2\pi/\omega_0} f(i)\mathrm{d}t\mathrm{d}i = 0. \tag{3.21}$$

where $v(t, t')$ is replaced for an arbitrary function of current, since,

$$v(t, t') = r(t')i(t, t') = f(i(t, t')). \tag{3.22}$$

The integrals in (3.21) can be evaluated separately since they are independent of one another, the function $f(i)$ is periodic in both ω_0 and ω_1, and each integral is over one period. All this together meaning that each integral evaluates to 0 as in [42].

Next, the summation must be examined, and is best done after expansion. Carrying this out, and then considering any arbitrary pair of indices and their negative counterparts, $\pm\ell_h$ and $\pm k_i$, looks like,

$$\begin{aligned}\sum_{\ell=-1}^{1}\sum_{k=-\infty}^{\infty} V_{k\ell}\left(-k^2\omega_1^2\frac{I_{k\ell}^*}{j(\ell\omega_0+k\omega_1}\right) &= \\ \cdots + V_{k_{-i}\ell_{-h}}\left(-(-k_i)^2\omega_1^2\frac{I^*_{k_{-i}\ell_{-h}}}{-j(\ell_h\omega_0+k_i\omega_1}\right) &+\cdots+0+\cdots+ \\ V_{k_i\ell_h}\left(-k_i^2\omega_1^2\frac{I^*_{k_i\ell_h}}{j(\ell_h\omega_0+k_i\omega_1)}\right) &+\cdots\ .\end{aligned} \tag{3.23}$$

Recall that by definition conjugate symmetry across frequency permits

$$\begin{aligned}V_{k_{-i}\ell_{-h}}I^*_{k_{-i}\ell_{-h}} - V_{k_i\ell_h}I^*_{k_i\ell_h} = V^*_{k_i\ell_h}I_{k_i\ell_h} - V_{k_i\ell_h}I^*_{k_i\ell_h} &= \\ 2\mathrm{Im}\{V_{k_i\ell_h}I^*_{k_i\ell_h}\} &= N,\end{aligned} \tag{3.24}$$

and then considering any two corresponding terms causes every pair to reduce to

$$\left(k_i^2\omega_1^2\frac{V_{k_{-i}\ell_{-h}}I^*_{k_{-i}\ell_{-h}} - V_{k_i\ell_h}I^*_{k_i\ell_h}}{j(\ell_h\omega_0+k_i\omega_1)}\right) = \left(k_i^2\omega_1^2\frac{N}{j(\ell_h\omega_0+k_i\omega_1)}\right). \tag{3.25}$$

By dividing out ω_1, recombining the summations, and acknowledging that carrying out both summations from $-\infty$ to ∞ would result in counting the harmonics twice and consequently dropping one side, the final expressions are

$$\sum_{\ell=-\infty}^{\infty}\sum_{k=0}^{\infty}\frac{k^2N_{k,\ell}}{\ell\omega_0+k\omega_1} = 0 \tag{3.26a}$$

$$\sum_{\ell=0}^{\infty}\sum_{k=-\infty}^{\infty}\frac{\ell^2N_{k,\ell}}{\ell\omega_0+k\omega_1} = 0, \tag{3.26b}$$

where the second ratio in (3.26b) comes from carrying out the analysis with (3.20) derived with respect to t instead of t'. If a linear, time-varying element is used, then $\ell \in [-1, 1]$, representing frequency content of the form $\pm\omega_0 + k\omega_1$. A nonlinear load, on the other hand, will also evoke harmonics from the excitation itself, resulting in $\ell \in [-\infty, \infty]$ and frequency content at $\ell\omega_0 + k\omega_1$ for any choices of k and ℓ.

3.6 Analysis

Unfortunately, both this and the MR reactive power relationships do not conserve power. The derivation is carried out using the imaginary part of the apparent power. In a linear system, this would be the reactive power and is described as such in [18]. However, in a nonlinear system, it is better described as nonactive power, and then by both the earlier and current definition, it is not necessarily conserved. In order to verify this, taking both (3.26a) and (3.26b), multiplying them by ω_1 and ω_0 respectively, and adding them together, the expression

$$0 = N_{0,1} + N_{1,0} + \sum_{k,\ell=1}^{\infty} N_{k,\ell}\left(\frac{k^2\omega_1 + \ell^2\omega_0}{k\omega_1 + \ell\omega_0}\right) + \sum_{k,\ell=1}^{\infty} N_{k,-\ell}\left(\frac{k^2\omega_1 + \ell^2\omega_0}{k\omega_1 - \ell\omega_0}\right), \quad (3.27)$$

is found. This is in direct opposition to power conservation that would require the reactive power at the excitation frequency, $N_{0,1}$, pumped frequency, $N_{0,1}$, all sum harmonics, $N_{k,\ell}$, and all difference harmonics, $N_{k,-\ell}$ to sum to zero. Instead, all harmonics require that they be adjusted by some ratio of the harmonic frequencies and indices to sum to zero. Additionally, by multiplying by ω_1^2 and ω_0^2 and carrying out the same steps the proof of unconserved power made by Manley and Rowe can be found.

3.7 Concluding Remarks

Moving forward, it needs to be remembered that nonactive power is not conserved and is ill-defined by current standards. There are, however, useful metrics by which to discuss the cross-frequency effects of nonlinear resistive elements and harmonics in general as described by the accepted IEEE definition. Moreover, there are alternative definitions that could be utilized in particular circumstances, but without widespread adoption their use is limited. While there now exist at least two power-balance expressions for nonactive power in nonlinear resistors, these cannot serve much use until conservation is reconciled by the adoption of a new understanding of nonactive power. As the AIEE conference had seemingly concluded nearly a hundred years ago - perhaps nonactive power is too convoluted a mechanic and for electrical engineers only serves as a quantity to be minimized and avoided.

This chapter and the previous one centered on analysis, but the next chapter will move into a more practical realm. No longer focusing on analysis, the thesis will now look into the physical limitations of an antenna design that utilizes nonlinear components. Through power testing, the linear assumption used in the design will be evaluated, and whether or not that assertion is correct will be verified.

Chapter 4

Limitations of Varactor-Based Reconfigurable Antennas

Reconfigurable antennas are crucial components of modern communication systems in congested and contested spectral environments [20]. These devices can undergo several different kinds of changes to update their behavior. Pattern reconfiguration is a method of increasing the gain in spatially active RF environments. A highly directive antenna that usually suffers in monitoring large angles can utilize pattern reconfiguration to achieve high omnidirectionality, usually only found in fewer directive antennas. Polarization reconfiguration is another spatial reconfiguration scheme that instead changes the polarization angle. These two will be referred to, in tandem, as spatial reconfiguration. The third, primary kind of antenna reconfiguration is frequency. In a tightly packed spectrum, an antenna can jump between operating frequencies to maximize its link budget. It is apparent how the implementation of any of these schemes increases the antenna's performance at a particular angle, polarization, or frequency but less obvious is that doing so also limits the interference of undesired sources. Spatial reconfiguration can also be used to avoid noise sources or interference from a particular angle or polarization, and frequency reconfiguration can greatly increase the signal-to-noise ratio (SNR) and mute unwanted sources nearby in the spectrum. In many different ways, an antenna can be made to update its behavior in real-time, there are even more ways to accomplish these tasks.

There are several methods for accomplishing these tasks [20]. Switches are often used in spatial reconfiguration to engage and disengage sections of a radiator. Motors can be used to give a greater degree of freedom in the movement of radiators, but come with SWaP-c drawbacks compared to switches. Microelectromechanical systems (MEMS) are a burgeoning field for reconfigurable antennas as they can mitigate much of the SWaP-c issues brought on by other mechanical tuning means. Stepping away from mechanical means, however, there is also the usage of variable reactance components. Here the investigation will be limited to variable capacitance, varactor didoes (varactors). Instead of minimizing the junction capacitance, these diodes are manufactured with much larger, predictable junction capacitance that changes with the bias voltage, thereby acting as a voltage-dependent capacitance. When used with relatively small RF voltages and a DC biasing network these devices are a cheap, small, and energy-efficient means of directly changing the resonating frequency of an RF structure. Unfortunately, they come with their disadvantages as will be discussed presently.

It is well known that varactors suffer from power handling issues with limitations in both overall power dissipation capabilities and nonlinear operation. An example is Skyworks' SMV1405-040LF varactors, used for the design shown here, with a relatively small power dissipation rating of 220 mW. Additionally, attempting to pass a meaningful amount of RF voltage, even if it maintains the power dissipation rating, results in time-dependent swings [23]. It will be shown here that this time-varying capacitance will damage the antenna's impedance match. Moreover, if the varactor operates at too high of an RF power it can also generate unintentional radiation at harmonics [21], [22]. Later, it will be shown where the intermodulation distortion comes from and its situational dependence. This work will corroborate these limited findings and continue their work by applying a harmonic distortion analysis to better measure the effects of the interharmonic distortion, and to better verify that the varactors themselves create significant distortion. Moreover, these will be compared against an antenna with an alternate tuning method, specifically a variable reactance controlled by a conductor attached to a stepper motor.

4.1 Modeling, Design, and Fabrication

4.1.1 RRELSA - Design 1

The varactor-based, frequency-agile antenna studied here was the Ring Resonator, End Loaded Slot Antenna (RRELSA) as described by [43]. The design was retuned to be centered around 4 GHz and tuned roughly from 2.5 GHz to 5.5 GHz. This required the antenna to be reduced in size significantly but allowed the ground plane to be reduced as well to permit two antennas per 9”x12” Printed Circuit Board (PCB) board. As will be shown in the first set of measurements, the RRELSA had to be used at 3 GHz to meet the circulator’s operation band. However, the RRELSA is most efficient towards the upper middle of its band and this places the RRELSA operating towards the bottom. This results in a very poor realized gain. Therefore, the RRELSA underwent a second design phase as shown in a later section. The first design was well-matched, as shown in Figure 4.2. It should be noted that the capacitances vary between the two, as 0.33 V was used to bias the line, ideally driving the varactors somewhere between 2.1-2.6 pF. In contrast, the HFSS simulation required a capacitance of 1.7 pF.

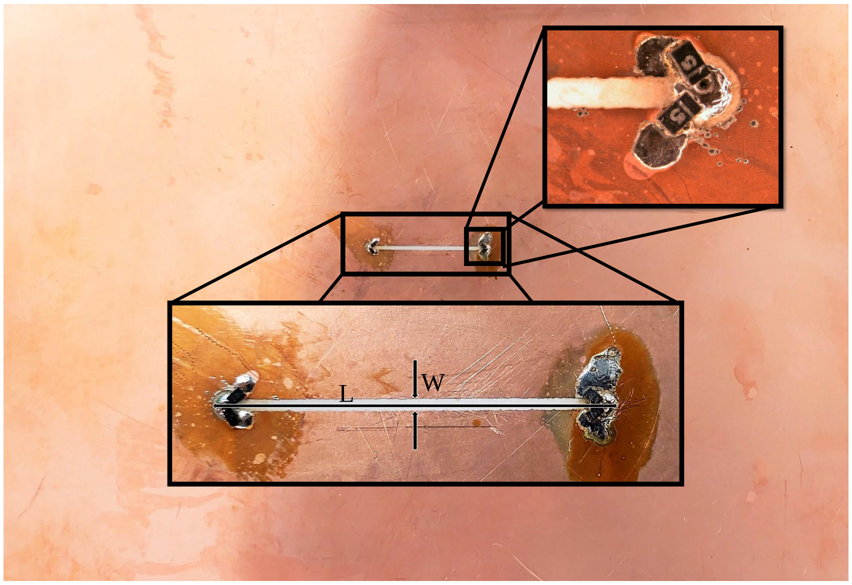

Figure 4.1: First fabricated RRELSA.

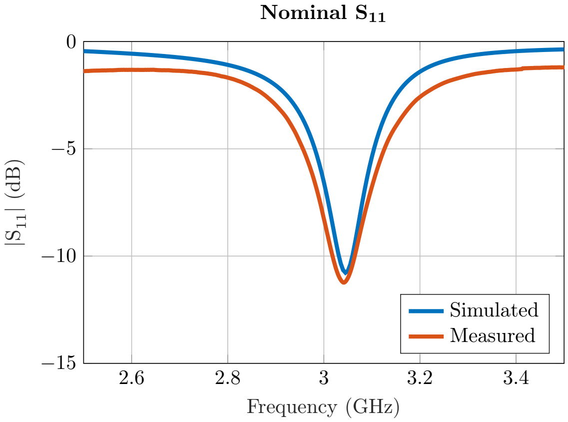

Figure 4.2: Nominal response of RRELSA.

Diode Analysis

The Skyworks varactor model SMV1405-040LF was used, as previously stated. This model allows for capacitances from 2.67 pF to 0.63 pF when a reverse voltage between 0 to 30V is applied. Using the manufacturer's SPICE model parameters femtoamps are expected when in reverse bias up to 30 V, and Skyworks states that when operating at the expected reverse bias voltages a maximum reverse current of 20 nA is possible. Since the varactor is nearly an open in reverse bias, any power dissipation that could cause the varactor to fail would be a result of positive RF voltage on the RRELSA. As the design is tuned using 330 mV, it would only require a relatively small amount of voltage to enter forward bias and instigate power dissipation. Figure 4.3 shows the voltage drop across the ring resonator at the location of one of the varactors when the varactors are all set to 2.2 pF, to mimic the expected time-invariant behavior when tuned to 3 GHz. Then using these voltage drops the varactors' nonlinear behavior was modeled using SPICE, with the circuit displayed in 4.4. Since the RRELSA and varactor placement is symmetric, this voltage drop can be assumed to be across any of the four varactors, and modeling one of them should be sufficient to describe any of them. The model used neglects the variable capacitance that shows up across the varactor when in reverse bias. A SPICE model that includes this capacitance does exist and is available from Skyworks, however, they warn that this model and the capacitance calculations used for the variable capacitance assume that the diode is not rectifying the signal. Since the point of this analysis requires heavy rectification, this model was not used. The model in Figure 4.4 is a sufficient first-order approximation to model the power dissipated and harmonics of the rectified signal, but moving forward it should be remembered that the frequency response may be slightly different in the absence of that capacitance. To understand where to expect nonlinear behavior and what powers the varactors can survive at, the varactor SPICE model from the manufacturer was used.

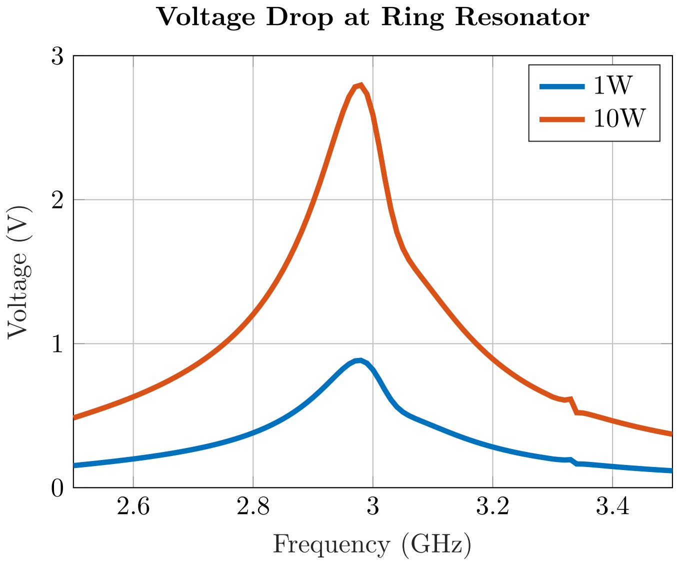

Figure 4.3: The voltage drop across the ring resonator at the location of one of the varactors. The voltage was calculated when the wave port was set to an excitation of either 1W and 10W.

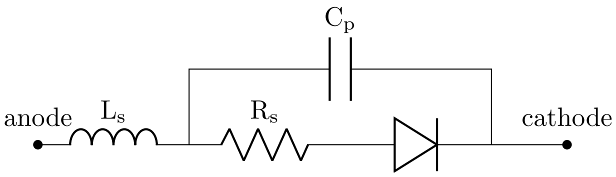

Figure 4.4: The spice model for the packaged varactor, the values used for the diode model were those described in the datasheet for this particular model.

The SPICE modeling was accomplished using Keysight's Advanced Design System (ADS) with a DC and transient simulation. The transient simulation with time gating was used to extract the steady-state, time-domain response of the varactor when the varactor model had either 0.9 V for the 1 W input condition or 2.6 V for the 10 W input condition. The RMS values were then calculated as they would express the average power the diode would experience, and these values are displayed in Figures 4.5, 4.6, and 4.7. It would seem that the average power sustained by the varactor when the input is at 10 W is 208 mW, just under the 220 mW limit cited by Skyworks. Upon examining the plots, however, it is clear that several harmonics will be generated by the varactor even at an incident voltage of 1 W. The measurements in a later section confirm this analysis.

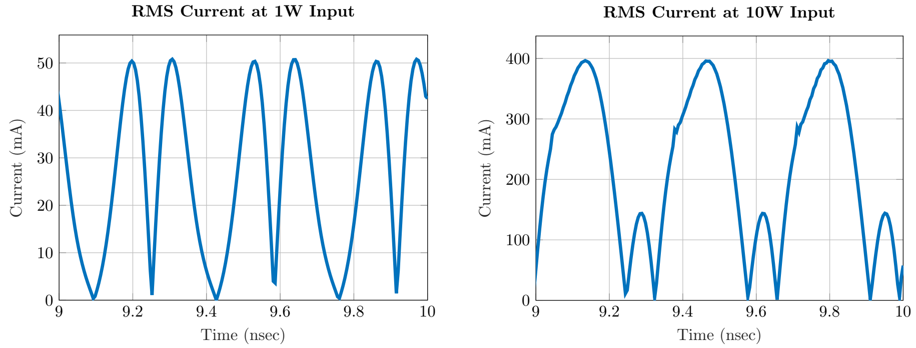

(a) (b)

Figure 4.5: RMS currents at the input of the diode model.

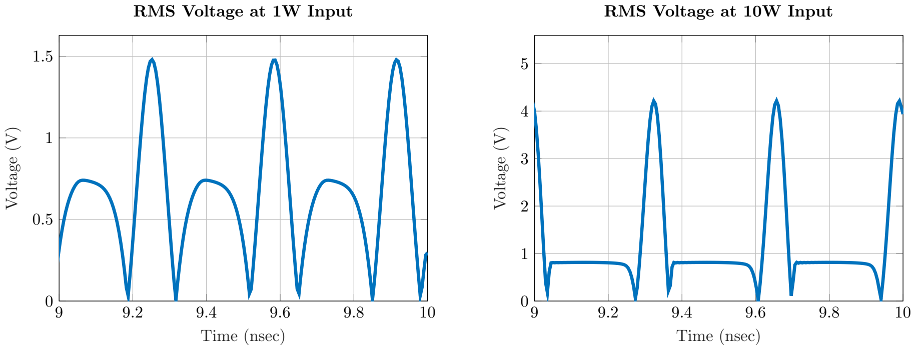

(a) (b)

Figure 4.6: RMS voltages at the input of the diode model.

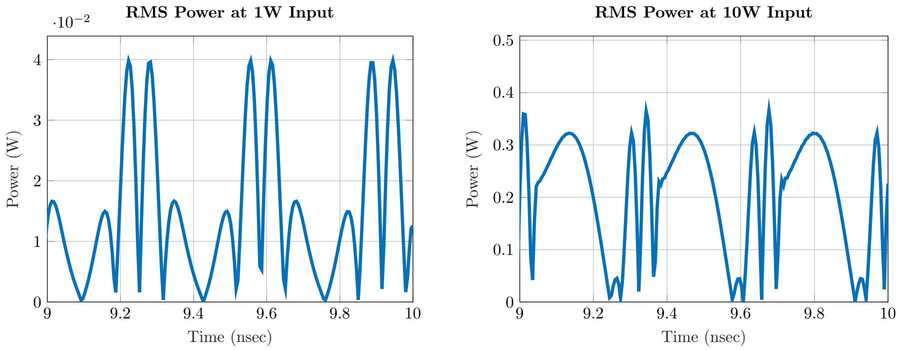

(a) (b)

Figure 4.7: The modeled power dissipation within the diode due to the calculated voltage and currents.

4.1.2 CBS

As the alternate tuning method to compare to the RRELSA, a cavity-backed slot (CBS) was used as detailed in [44]. This antenna uses a New Scale Technologies M3-L Micro Linear Actuator to finely adjust a copper disc that sits at the aperture of a slot antenna. This disc adds a capacitance across the slot, and by moving it across the aperture of the slot the reactance, and therefore the resonant frequency, is changed. The slot itself is fed with a hemispherical cavity, that is in turn fed by an edge launch coaxial connector using a co-planar waveguide. The antenna was fabricated using an LPKF S104 mill for the vias to create the cavity and the opening for the slot, and photo-lithography to remove copper from one side of the PCB that made up the slot ground. The response of the CBS tuned to 3 GHz and the CBS used are shown in Figure 4.8.

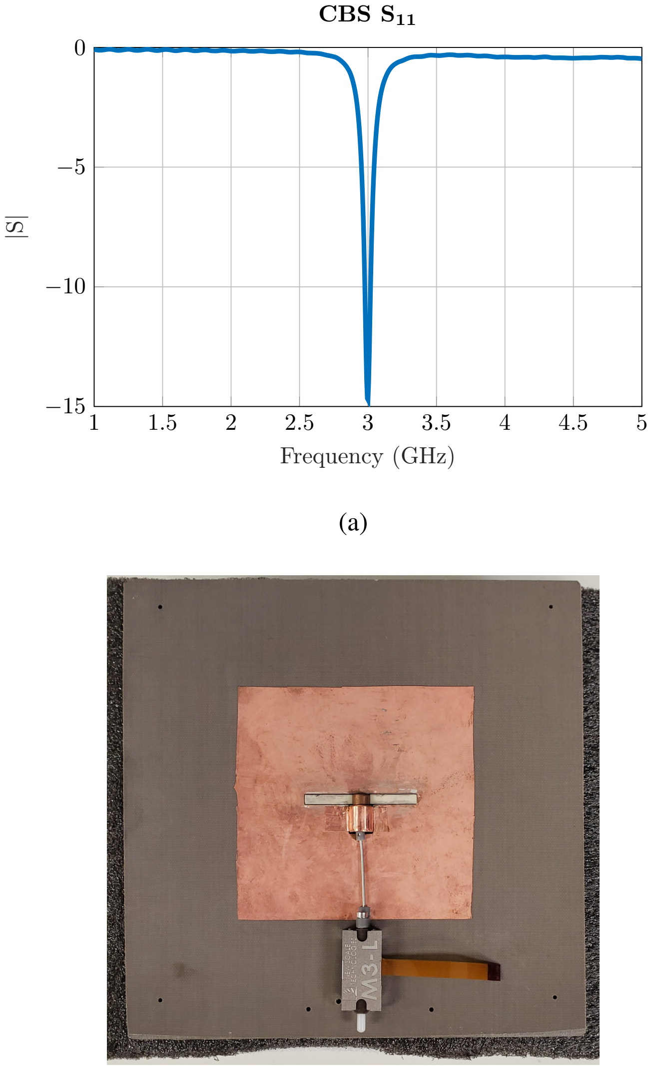

(a)

(b)

Figure 4.8: Tuned, nominal response of the CBS and a picture of the fabricated antenna

4.1.3 Low Pass Filter

Initial results of the experiments led to the realization that the harmonic distortion from the amplifier would not necessarily be negligible, and at this point there was no filter within the amplifier's chain. To further reduce the effects it was decided to place the low pass filter within the front end. A stepped impedance filter was used as it can push undesired resonances much higher in frequency than other filters that employ resonant structures [45]. A lumped component filter was considered at first as it would ideally dissipate less power being largely reactive. However, the stepped impedance was settled upon as no special care would be required to protect the filter as the Rogers 3003 it was to be built on could handle the power and any thermal energy. It was designed to have a cutoff frequency of 3.5 GHz, use a fifth-order polynomial, and match to a 50 Ω system. The coefficients used are in Table 4.1.

g_0	g_1	g_2	g_3	g_4	g_5	g_6
1.0000	0.6662	1.2445	1.4731	1.2445	0.6662	1.0000

Table 4.1: Coefficients used for the prototyping of the stepped impedance low pass filter.

There were a few drawbacks to this filter as well. Primarily it has a poor roll-off and requires more orders than other kinds of filters to have an acceptable transition from passband to stopband. Additionally, the use of narrower lines improves performance but can make fabrication more difficult, as the increasingly narrow inductive lines cannot suffer much change in width and are somewhat delicate. Despite these drawbacks, the design worked great as shown in Figure 4.9. The filter itself was fabricated using photolithography on a Rogers 3003, 60 mil board, and fed to 50 Ω microstrip line to coaxial edge launch connectors.

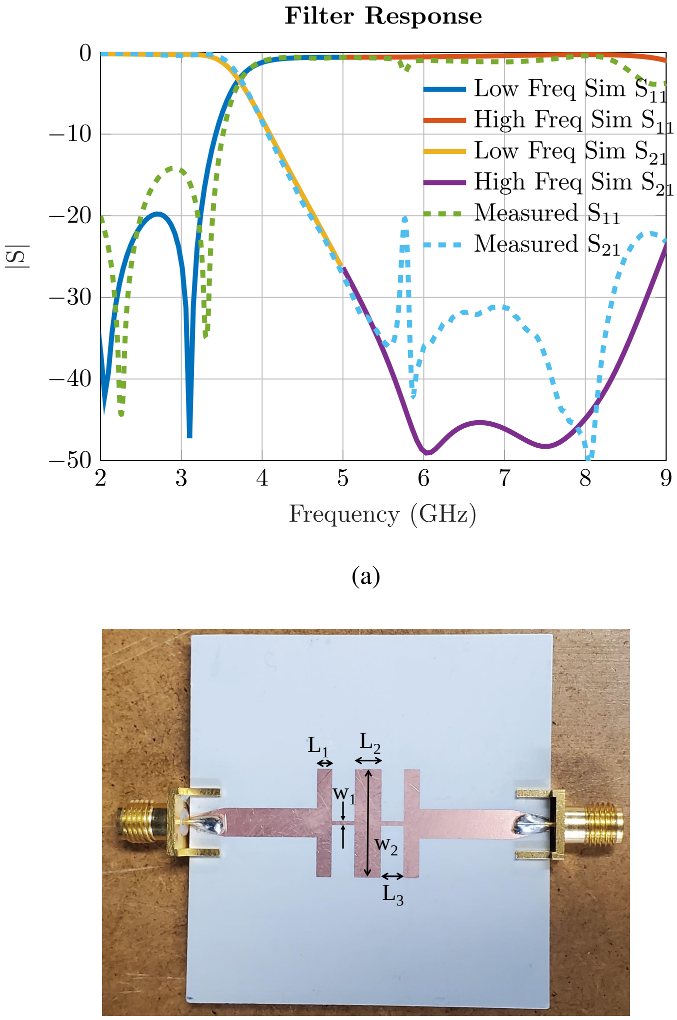

(a)

(b)

Figure 4.9: The response of the filter and a photo of the fabrication results. The dimensions are W_1 = 1.016 mm, W_2 = 16.51 mm, L_1 = 2.25 mm, L_2 = 4 mm, and L_3 = 5 mm.

4.2 Experiment Setup

4.2.1 Equipment

The measurements revolved around a front-end specifically designed for power testing RF components. A Keysight-Agilent E8267D signal generator was used as an input device, that then fed a Comtech BME2969-100 amplifier, capable of 59 dB of gain, up to 100 watts. The output of the amplifier then led to an RFCI RFCR8853N circulator, whose limited passband dictated that the measurements be taken at 3 GHz for the best results. The third port of the circulator led to a BW-30N100W+ pi network attenuator, rated for 100W. The second port of the circulator fed to a Mini-Circuits ZGBDC35-93HP+ bi-direction coupler that was conditioned by a fifth-order stepped impedance filter with the response shown in Figure 4.9. This would reduce the harmonic interference from the amplifier, and make it easier to ascertain the harmonic behavior of the antennas. The output on the main line fed the transmit (TX) antenna. The coupled side was used to make measurements on the TX side, with two different coupled directions to measure either the output from the circulator or the reflected wave from the antenna. The bi-directional coupler had one of two spectrum analyzers hooked to it depending on the measurement taking place. A Keysight-Agilent EXA Signal Analyzer, with a spectrum analyzer application, was used on the input to measure the response from the bi-directional coupler and to measure the reflected wave from the antenna. These measurements would not be done in tandem, as the analyzer had only one port. This also allowed the same port, connectors, and cable to be used between measuring the incident wave and the reflected wave to get as close to a calibrated response when measuring S_{11} without re-deriving calibration standards. All loss in any measurements that were taken and the coupler's response were also calibrated out. When the radiated power was being measured, regardless of what antenna was where, the signal analyzer was used on the receive antenna instead of the coupler. In these instances, a Tektronix RSA6114A spectrum analyzer was used to inspect the amplifier during testing to ensure it was behaving correctly. Any time there was not an analyzer attached to the coupler, 50 Ω loads were used to prevent erroneous reflections. Finally, measurements were handled using a Dell Precision laptop and managed Standard Commands for Programmable Instruments (SCPI) python scripts to automate the data capture. It was always hooked into the signal generator and the signal analyzer and was not used with the Tektronix spectrum analyzer. All measurements were taken in the Advanced Radar Research Centers' Far-Field Anechoic Chamber, and whenever a measurement was taken to check tuning and nominal performance or determine system losses, a Fieldfox N9928A network analyzer was used. As a final note, the data cables and coaxial cables used limited the configurations, unfortunately, and limited the transmit chain's possible placements. There were also several antennas, both under test and not, that were incorporated into testing as well.

Six antennas in total were used, three of which were antennas under test (AUT), and three were standard gain horns. The AUTs were the RRELSA designed for this experiment, a CBS, and a Narda 652-15 standard gain horn to act as a control for the experiment. This horn was also used as a TX antenna on one setup. The Narda 652-20 was replaced with a Narda 654-20 to measure harmonics of about 6 GHZ and a Narda 659-20 to measure any of about 9 GHz. While this list includes all of the major instruments and resources needed, they were used in a variety of setups to record different data.

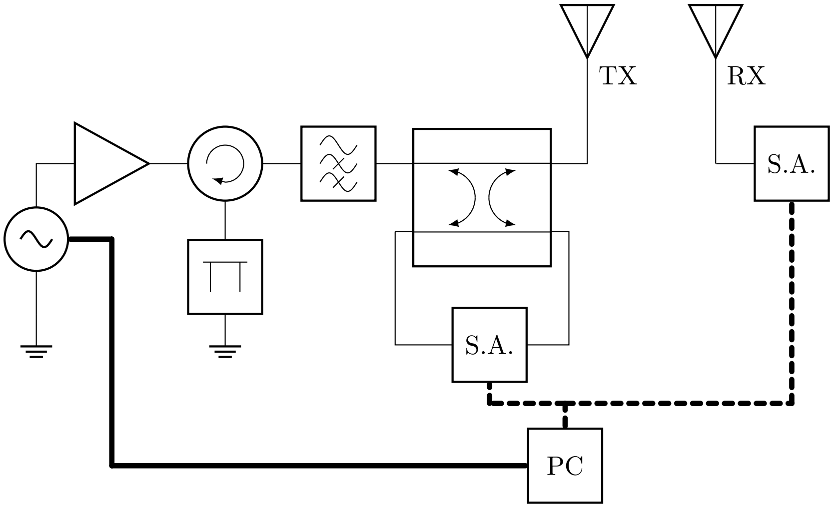

Figure 4.10: Block diagram of the RF front end used for the RRELSA experiments.

4.2.2 Configurations

Three equipment arrangements were used to accomplish the experiments. The first involved a receive (RX) antenna with no TX antenna, placing the signal analyzer at the coupler and not an RX antenna. This setup was used to measure the reflection from the AUTs across various incident powers and frequencies. In this case, the laptop would do one of two things: First, set the signal generator to 3 GHz and sweep through different power levels, and would capture the data from the signal analyzer at each power level. Second, it would set the signal generator to a specific power level, sweep across frequency while capturing the response at that frequency from the signal analyzer, and then do it over again at different power levels. The first captures match degradation across power while the second more closely examines what the return loss is doing at different power levels. This arrangement was also used to directly measure the transmit chain's output, by using a BW-N30W20+ attenuator to terminate the coupler in a 50 Ω load. The measurement recorded from the incident wave to the coupler was used to remove the harmonic distortion of the amplifier itself from these measurements. For these measurements the AUTs were placed almost directly to the coupler with minimal cable and connectors, this greatly improved the measured response as shown in Figure 4.11. This also meant that the AUTs would be placed on the catwalks and not on either pedestal. Since radiated power was not of much concern, this was not considered to have a great impact on the measurements. In this state, the chamber did more to shield the outside from EMI as opposed to providing a quiet environment. There were initial tests done with the instruments outside the chamber, however, the interference at 3 GHz was far too great. Most of the equipment showed to have little effect on the antenna by being that close. There was, however, a noticeable shift upwards in resonant frequency when the RRELSA was attached to the front end and was retuned to compensate for the shift. Two other configurations were used to measure the power radiated by the antennas in question.

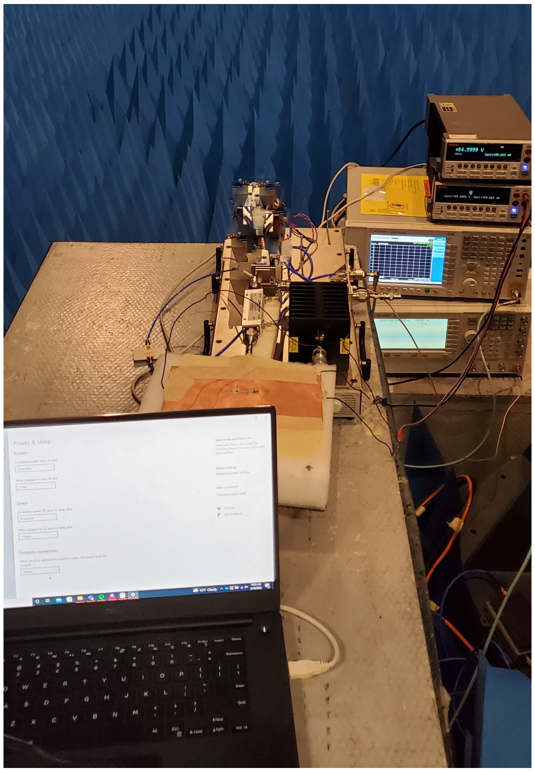

Figure 4.11: Photo of the power testing setup for the reflection measurements.

Another configuration placed the AUTs as the TX antennas and a 3 GHz horn as the RX antenna as shown in Figure 4.12. This puts the signal analyzer on the RX antenna. In this case, the PC would trigger the signal generator to send out a 3 GHz tone at increasing power levels and would capture the response on the RX antenna from the signal analyzer at the fundamental frequency. The 3 GHz horn was then swapped for the 654 and the first harmonic at 6 GHz was captured across the power levels. This was then repeated a third time with the 659 for the second harmonic. The signal analyzer was used to also capture the output of the amplifier while each antenna was hooked up, like in the first configuration. The input measured when the horn was attached could be used to separate the response of the amplifier from any harmonics generated by the antennas themselves. For this setup, the AUT was placed on one pedestal and the RX antenna on the other. It required a significant amount of cable and routing through the bulkhead, but the laptop was able to connect to both the signal generator and analyzer to automate the experiment. This loss was calibrated out, and the AUTs being on TX ensured that they would receive the full power of the amplifier to elicit any nonlinear behavior.

The third configuration placed the Narda 654-20 as the transmit, and either the CBS or the RRELSA as the RX antennas, with the rest of the equipment setup like the second configuration. The antennas would be placed in the same locations as in Figure 4.12. The same measurements at the fundamental, first, and second harmonics were taken. This configuration was the most hampered by cable and facility limitations. The transmit chain had to stay on one side, as the instruments could only be safely placed on one side of the chamber without copious amounts of cable loss between the amplifier and the AUT. This meant that the AUTs in receive would suffer both propagation loss and the +20 dB in cable loss from the AUT to the signal analyzer. The power received would limit any nonlinear behavior, and cable loss could hide that below the noise floor. This setup was also used to measure the RRELSA radiation pattern, as the pedestal on this side of the chamber had an azimuthal motor to rotate it around.

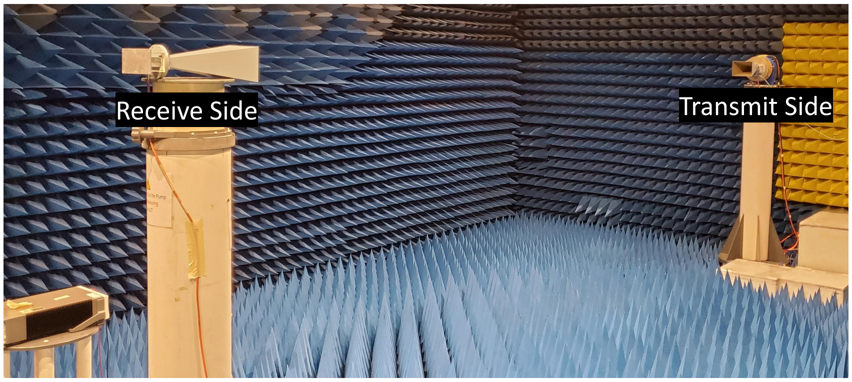

Figure 4.12: Picture of the over-the-air measurements taken in the anechoic chamber.

4.3 Measurements

4.3.1 Reflection

The first measurements taken involved the reflected voltage waves from the AUTs using the first configuration. Figure 4.13 shows the effects of input power on the AUTs. The horn is used as a control and consistently has an S_{11} of -10 dB. The CBS also maintains a steady reflection across power, and its higher Q against the horn is apparent in the -14 dB improvement in reflection. The RRELSA does not perform nearly as well across frequency, however. At -30 dBW the reflection is acceptable, but even in the tens of milliwatts the varactors damage the antenna's input impedance too greatly for it to be effective at the ideal operational frequency, and appears to balance out at just a couple dB down from total reflection. Figure 4.13 also illuminates what is happening to the antenna's resonance as the input power changes. Very quickly there is a shift upwards in the S_{11} minimum, and much before a full watt is incident the operational frequency is far gone from the needed band. Therefore, the RRELSA's mismatch efficiency cannot withstand much more that -30 dBW and still meet basic tolerances. It seems then that it would require an exotic matching network to permit operation across much of the desired bandwidth.

These reflection coefficients were acquired by simply sweeping through the power and measuring one of the coupled inputs from the coupler while terminating the other in a 50 Ω load, and then swapping the spectrum analyzer and the load to get the other quantity. This should effectively only leave the response of the antenna, the connector from the coupler to the antenna, and the coupler's response in these measurements. Ideally, the coupler would be ultra-wideband and perfectly flat, but that is not the case as shown in 4.13. Despite the passband ripple, however, the mismatch efficiency degrades. If anything, the ripple and imperfect isolation between the input and output on the coupler makes the antenna appear to perform slightly better when it is mismatched due to higher input powers. This configuration was also used for another kind of reflected voltage measurement.

Figure 4.14 demonstrates that the issues do not stop with a rapidly decreasing mismatch efficiency and extend to wholly nonlinear effects as well. Here, both the horn and the CBS succeed in having limited interharmonic distortion. In this figure, the amplifier voltage at each harmonic has been subtracted out to emphasize the behavior of the RRELSA. However, harmonics are generated from the varactors on the RRELSA and then sent back through the front end. Figure 4.14 uses THD^{v} to inspect this issue, and in this context, the harmonic distortion is gaining exponentially. This all means that even if a dynamic matching network was used with the RRELSA there would still be interharmonic distortion to take care of as well. The reflected harmonics could be captured by a filter, but this would only protect the front end and would not stop the harmonic generation on the antenna itself.

There is one discrepancy within Figure 4.14, in that at two points there seems to be an upswing in the harmonics and they both coincide with a flattening of the slope in the reflected voltage at the fundamental. This could imply that the CBS is causing some harmonic behavior. The issue at the lower end is most likely measurement error, as those powers should be far too small to evoke any nonlinearity within the media. However, at the higher end, there is a possibility that there is some apparent nonlinear behavior occurring and moving power from one frequency to another. This can be a result of the considerable heat dissipation, as resistance is a function of heat and can create nonlinear behavior in resistances. The CBS did noticeably heat up during measurements, but an accurate measurement could not be acquired as the infrared thermometer could not handle the RF output power. Its capabilities for testing were briefly evaluated in chapter 5.

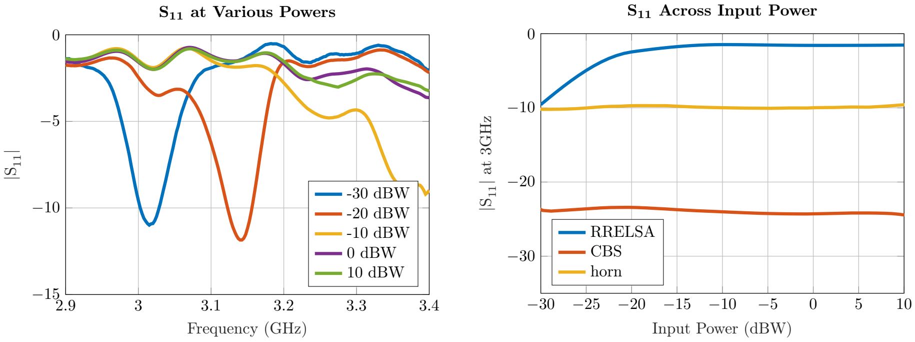

(a) (b)

Figure 4.13: S-parameters of the AUTs.

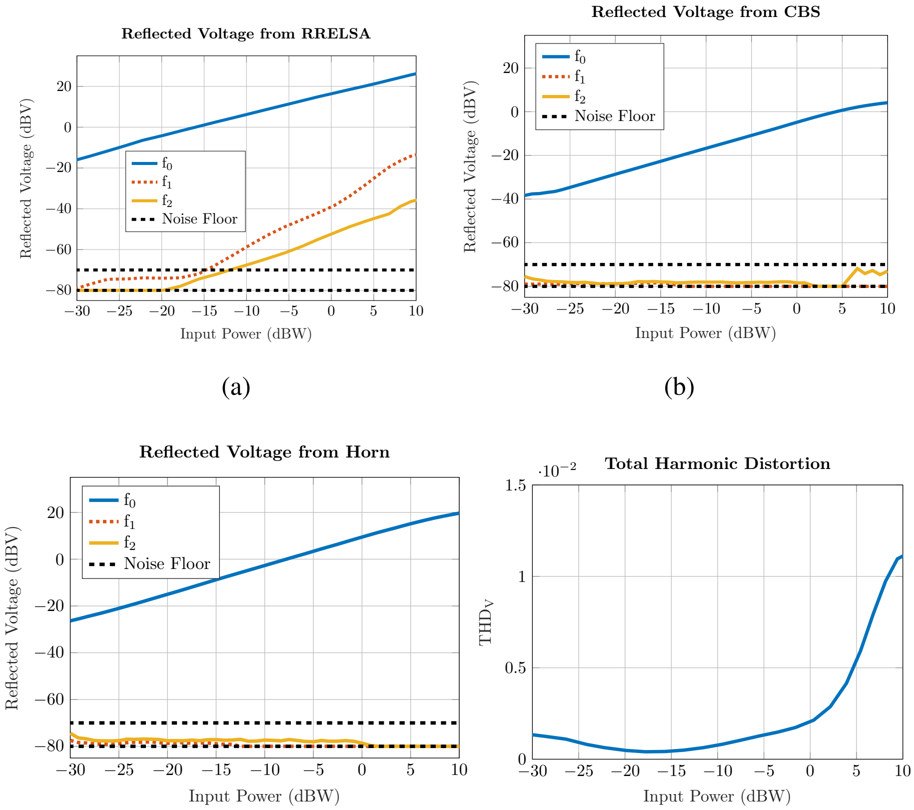

(a) (b)

(c) (d)

Figure 4.14: Reflection of the AUTs across harmonics.

4.3.2 Radiation

There are also concerns with radiated harmonic distortion as it can pollute the spectrum. Figure 4.15 shows the results of the AUTs operating as transmitters. In Figure 4.15a the horn and CBS are unaffected by the input power in terms of realized gain, however, that is not the case for the RRELSA. This is to be expected in part due to the mismatch generated by the change in input power. There is another source of the gain reduction, as shown in Figure 4.15b and 4.15c. It is important to note that the harmonics from the amplifier were not subtracted out here as there was not a straightforward, practical way to do so. The measurements show that the RRELSA did generate some harmonics above what was just generated by the amplifier, as indicated by the horn and CBS. However, what is to say that the differences here aren't merely a result of the gain of each AUT at those higher frequencies? With the same data, the conclusion could also be reached that the RRELSA has a slightly better gain at the harmonics than the other two. There are two observations that, despite possible differences in gain, affirm these harmonics were generated in the RRELSA and are not just a product of the amplifier. Firstly, there is a significant decrease in realized gain at the fundamental, and by extension transmitted power, by the RRELSA. If all three AUTs are given the same stimuli and there were no observed ohmic losses in the RRELSA, then power conservation requires the power missing from the RRELSA in Figure 4.15a must have gone somewhere. It was shown earlier that these varactors will create harmonics thereby moving power from one frequency to another, so it can be reasoned that the power difference at the harmonics was the destination of this power. Secondly, and perhaps less intuitive, is that there is power being generated at the harmonics in the RRELSA before the amplifier has delivered power to those harmonics. Figure 4.15d clearly shows that when the power transmitted is considered in terms of harmonic distortion the RRELSA is generating far more than the other two, and well before the amplifier begins to distort the output. It can be safely concluded that at certain powers varactor-based antennas will distort signals and pollute the spectrum.

These measurements were acquired using the second configuration, where the AUTs transmitted and one of three horns were used to capture power at one of three frequencies - the fundamental, the first harmonic, and the second harmonic. The power transmitted was found using a link budget between the two antennas, where

$$P_{tx-ant} = P_{tx} + G_{tx} = P_{rx} - G_{rx} + L_{loss} + L_{path} \quad \{dBW\}, \qquad (4.1)$$

where P_{tx-ant} is the power leaving the transmit antenna, P_{tx} is the power at the input of the transmit antenna, G_{tx} is the gain of the transmit antenna, G_{rx} is the gain of the receive antenna, L_{loss} is the loss in the cables, average loss in the coupler (if applicable), and loss in the bulkhead of the chamber, and L_{path} is the path loss between the two antennas, where L are negative quantities and G are positive. Additionally, all gain referred to in this section is realized gain. By subtracting the right side by the power from the amplifier the gain can be solved for any of the AUTs. All these loss terms and gain of the measuring horn were calibrated by taking the measurements between the two standard gain horns, the 652-15 and 652-20, and using that as the standard. The higher frequencies were adjusted for path loss recalculated at whichever frequency and cable loss was measured at each harmonic. By subtracting out the 3 GHz components and adding in the 6 GHz or 9 GHz components.

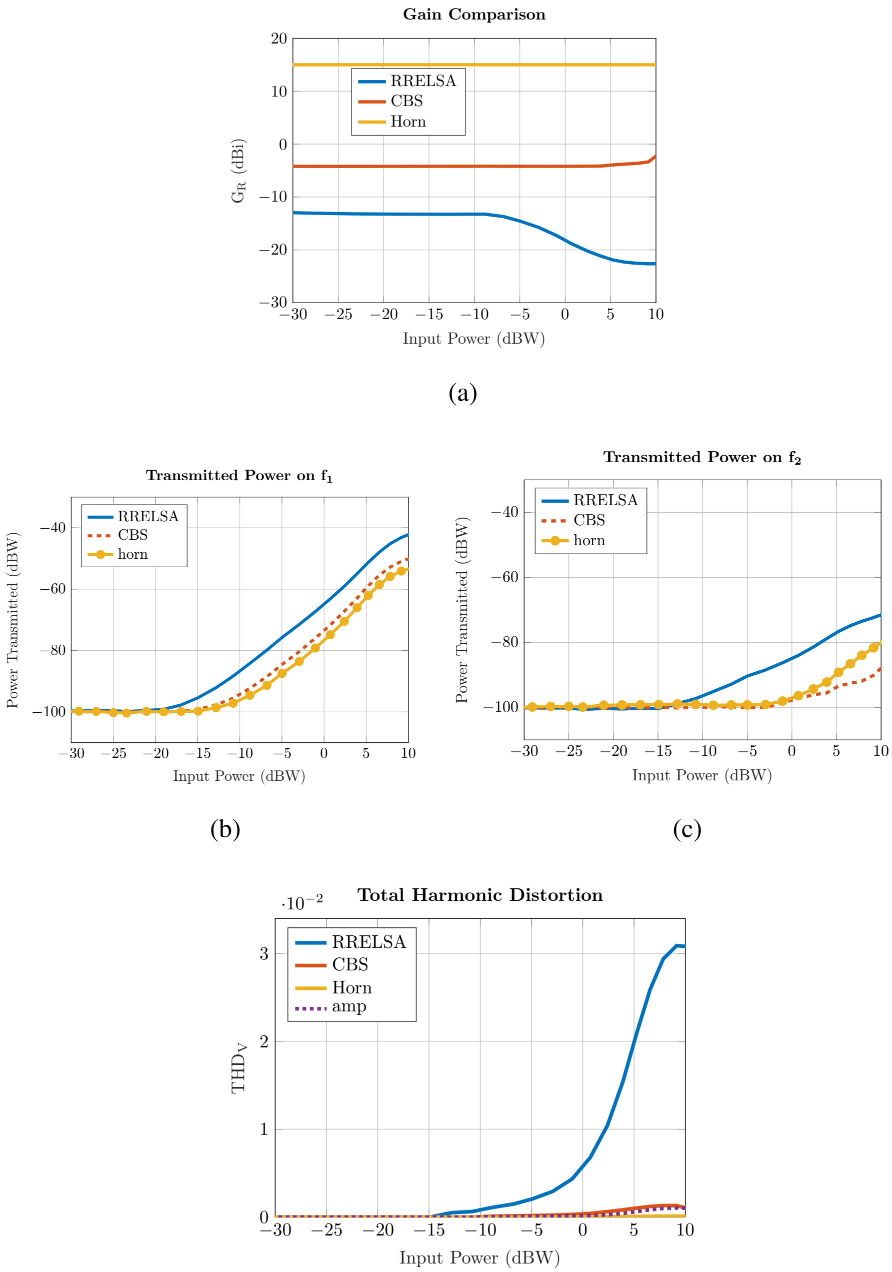

(a)

(b)

(c)

(d)

Figure 4.15: Power transmitted by AUTs across harmonics.

There could also be issues with the AUTs generating harmonics as receivers, which is the more likely scenario for practical uses for varactor-based antennas. In this case, the RRELSA does not generate significant harmonics relative to the other two antennas, as displayed in Figure 4.16. Surprisingly enough, the horn does a better job of receiving the harmonic transmitted by the TX horn than the RRELSA does of both receiving and generating the harmonic at 9 GHz. Additionally, the change in power does not seem to affect the radiation pattern either. Therefore, in the case of a 10W, with a high gain transmitter only 7 meters away, the RRELSA will do just fine as a receiver in terms of interhamronic distortion. Additionally, it seems that the agreement between the maximum realized gain in simulation versus measurements shows that the ring resonators are behaving similarly despite the difference in loading capacitance. This is most likely due to fabrication errors.

These measurements were calculated the same as in (4.1). It should be noted that gain on receive antennas assumes reciprocity which cannot be presumed in a nonlinear system. However, there were no harmonics outside the amplifier noticed, so standard gain calculations are acceptable for this case.

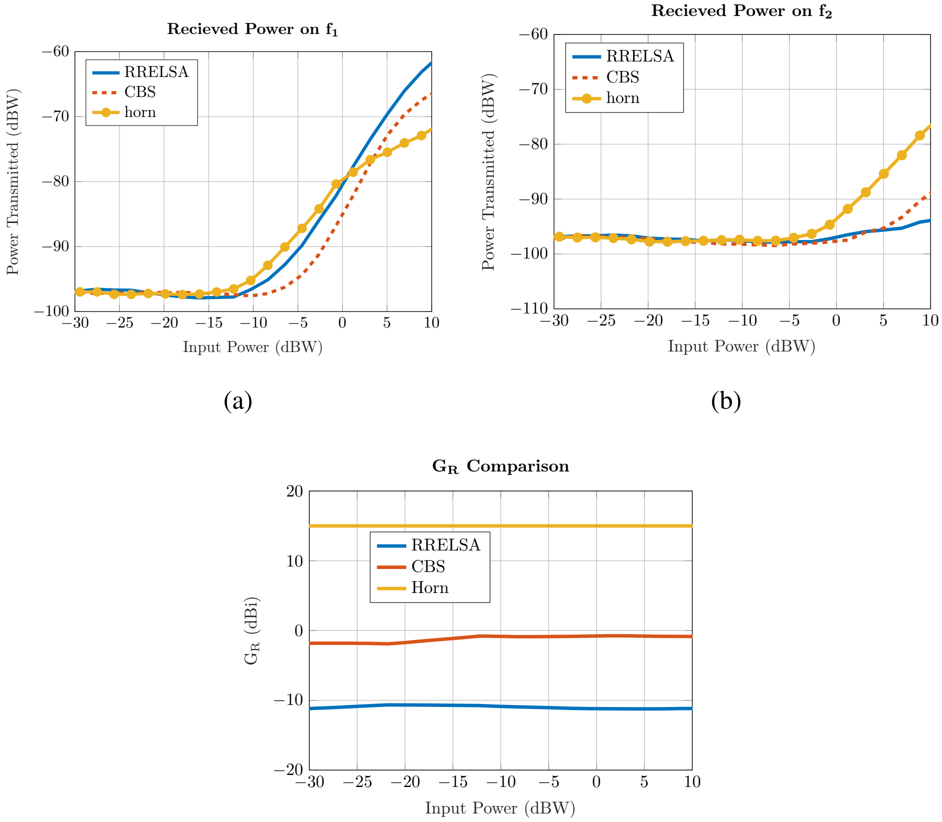

(a)

(b)

(c)

Figure 4.16: Power received by AUTs across harmonics.

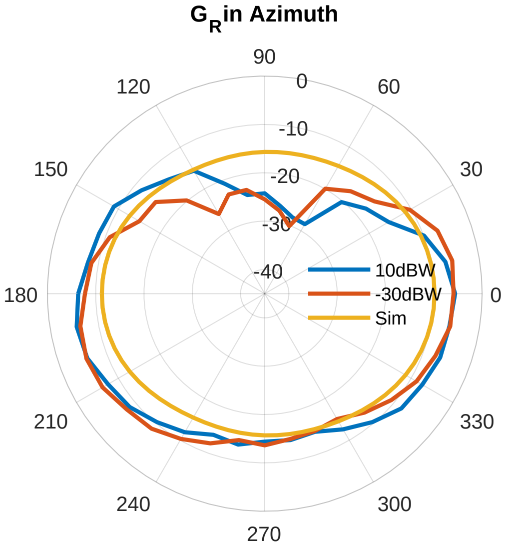

(a)

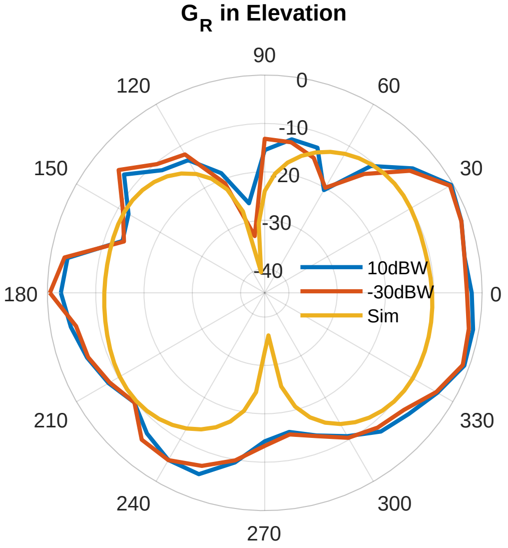

(b)

Figure 4.17: Gain pattern patterns of first RRELSA.

Despite the impacts of the nonlinear behavior at higher powers being evident in these measurements, there is one major issue with the second and third configurations. The realized gain is incredibly poor, sitting at -5 dBi in Figure 4.15. The effects of this issue on interharmonic distortion should be minimal when the RRELSA is set to transmit, as it is electrically large at the harmonics already and a slight alteration in dimensions and the varactor capacitance won't change that. Although, the change in DC bias may influence the harmonic behavior as operating at a significantly lower DC voltage will require a larger RF voltage to overcome the DC offset and begin rectifying against the varactor. Changing the efficiency will also affect the response of the RRELSA when it is in a receive configuration, as the RF power flowing through the varactors will increase with the change in radiation efficiency. Therefore, the next section will focus on another RRELSA, this time designed for a lower frequency to allow for better realized gain.

4.4 Redesigned RRELSA

The redesigned RRELSA was much closer in design to the original in [43]. It was slightly tuned higher in frequency, but the DC bias lines and feed were left untouched. Overall, the same fabrication methods were used for this design as the last one - the results of which can be seen in Figure 4.18. Unfortunately, the original choice of DC bias lines and pads was very fragile and suffered damage that had to be rectified with copper tape. This failure explains the erroneous dip in S_{11}. Experience with the first version showed that the feed needed solder down its length to keep the trace from popping from the substrate. Later versions should have a meaningfully updated DC trace and feed to give them more structural rigidity to better quality control the pattern and the input impedance. This will sacrifice the impedance matching from the coax to the feed line and the radiation pattern. Additionally, it was observed in the simulation that the RF voltage across the varactors was only 1.2V, so with a DC offset of 3 volts, we may expect to see less rectification.

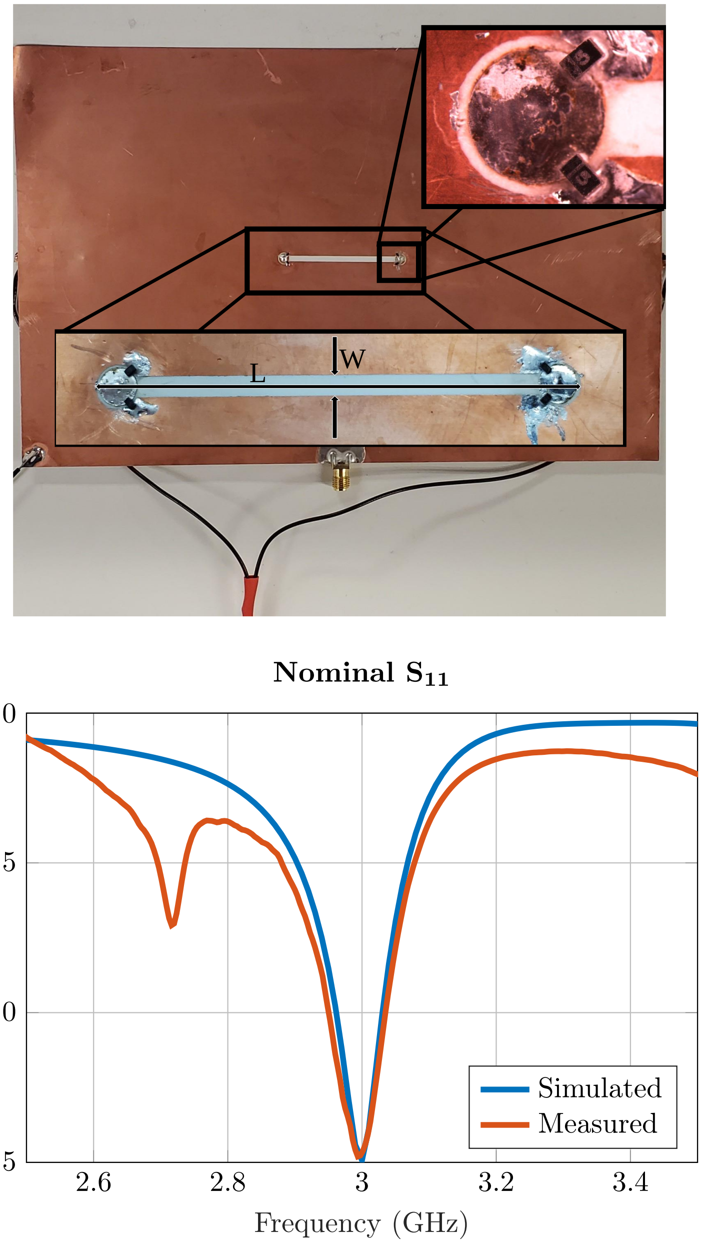

Figure 4.18: Second version of the RRELSA, with W= 0.7mm and L=21.8mm.

4.4.1 Redesign Results

The results for the redesigned RRELSA are similar to those in the first design. The RRELSA here detunes with frequency as well, except with a key difference. The earlier RRELSA had its match shift upwards in frequency as power increased, however here it shifts downwards. It would be expected that each one might detune slightly differently, perhaps with different rates or bandwidths, but in the other direction entirely is less expected. This may signify a different source of the detuning. as it was evident the first RRELSA experienced significant rectification. With a much lower DC bias and smaller RF voltage rectification was assumed to be less prominent. Figure 4.20 shows that this seems to be the case. Even at 10 W, there is nearly no noticeable rectification. While this model cannot handle the time-varying capacitance, it does show that there is still plenty of mixing due to the nonlinear nature of the diode. The frequency-domain analysis reinforces both points that the time domain shows, increasing the negative DC bias results in less harmonic generation, but does not completely remove it despite the prevention of rectification.

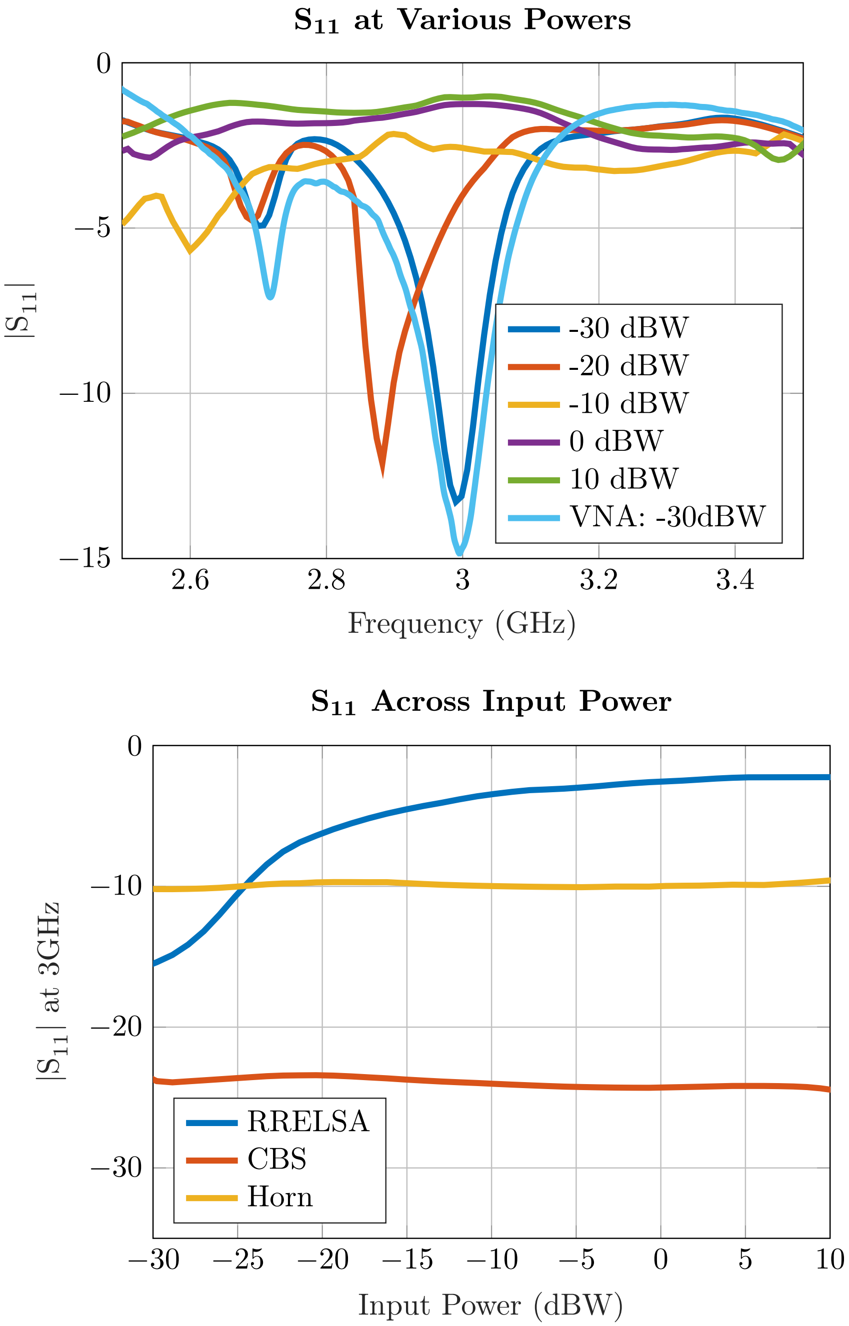

Figure 4.19: S-parameters of the AUTs with teh second RRELSA.

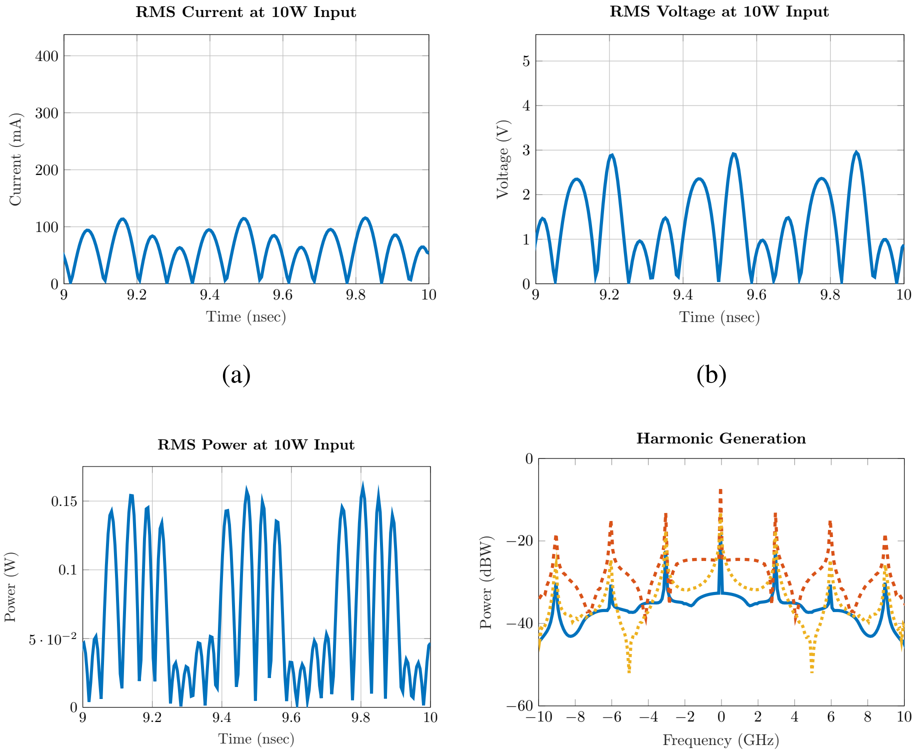

(a) (b)

(c) (d)

Figure 4.20: RMS currents at the input of the diode model.

Unfortunately, the time restriction on measurements prevented good transmit results from being procured. While they were taken, they appeared very poor. This most likely resulted from a simple measurement error. However, acceptable receive measurements were taken, as shown in Figure 4.21. Not only does the significant increase in radiation efficiency not damage the response on receive across the measured powers, but the pattern better matched the simulated results from HFSS. The only major discrepancy was the unintended null in the azimuthal plane. This was a result of the presence of the DC bias cables that were not included in the simulation - as this was the side the cables were laying on. While there is no definitive evidence about the performance in transmit, it appeared that the RRELSA will work well at these powers and distances.

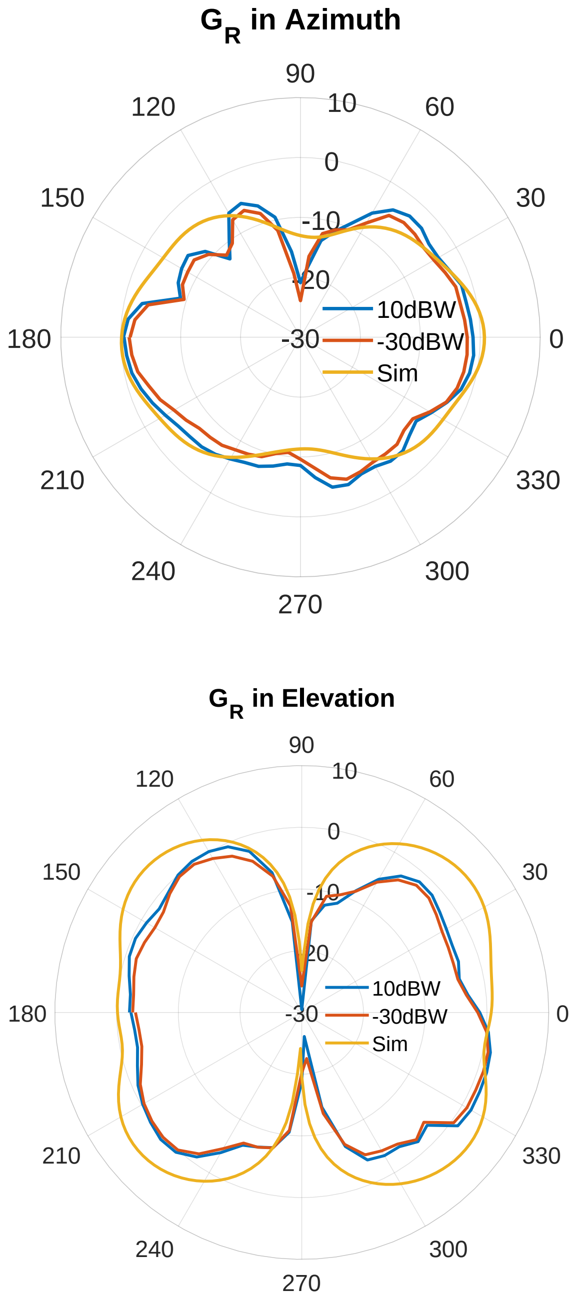

Figure 4.21: Gain patterns of second RRELSA.

4.5 Concluding Remarks

Varactors are an attractive variable capacitance but come at a cost. When in receive the linear assumption has been confirmed to be correct in the case of the RRELSA. It is important to consider not only the spectrum pollution brought on by the harmonic distortion when the varactors become nonlinear. Diodes, in general, have significantly different impedances with varying power levels, and even if they are not rectifying and generating harmonics that way, there are still other ways to generate harmonic distortion and complicate the system. The mismatch efficiency and the time-varying capacitance of a varactor will hamper the antenna's performance despite the mitigation of rectification. Aside from varactor-based antennas, there is another novel antenna design solution that could suffer from nonlinearity. Ferrite material has promise in being a solution to patch bandwidth issues, specifically substrates with magnetic properties. However, the magnetic material can behave ideally when higher powers are used. The next chapter investigates the possible power limitations of magneto-dielectric substrates for use with patch antennas, and how the magnetic bias could damage performance or generate harmonic distortion.

Chapter 5

Magneto-Dielectric Substrates

Microstrip patch antennas are a widely popular, planar antenna due in part to a phenomenal SWaP-c [46]. Like any antenna, however, they come with some drawbacks. Patch antennas operate with the best bandwidth when the distance between the patch and the ground plane is impractically large and the characteristic impedance is high. However, for the best efficiency, the distance between the patch and the ground plane must be reduced. Therefore, practical designs for patch antennas are left balancing between the two. Since patches are chosen for SWaP-c limitations, most designs opt to shrink the substrate height and increase the permittivity to reduce the impact of that choice to meet form factors. This leaves both efficiency and bandwidth severely reduced. These design necessities demand solutions to improve either or both of these quantities. One solution was detailed by Hansen, wherein ferromagnetic materials were theorized to alleviate the bandwidth issues and greatly improve the miniaturization of the patch antenna [24].

In Hansen's brief analysis in [24] he uses zero order analysis methods to investigate the effects of permeability and permittivity on a patch antenna's bandwidth and size. The results of the calculation found that the bandwidth of a patch could be described with,

$$\text{Bandwidth} = \frac{96\sqrt{\frac{\mu}{\epsilon}}t/\lambda_0}{\sqrt{2}(4+17\sqrt{\mu\epsilon})}. \tag{5.1}$$

According to this expression, simply increasing μ is not sufficient for bandwidth gains. Both μ and ϵ must be increased and at relatively equal values. However, if they are too large the denominator will become too large and negate any bandwidth increases. Additionally, in [24] it also described how the reactance generated by the inclusion of the permeability will permit miniaturization without harm to the bandwidth, unlike permittivity. Miniaturization will occur at a rate of $\lambda = \frac{c}{f\sqrt{\mu_r\epsilon_r}}$ in accordance with [47], while the presence of μ in both the numerator and denominator of 5.1 prevent significant impact to bandwidth with arbitrarily large values of μ.

Verifying the expectations in [24] and [47] expectations will be one goal of these measurements. Another will be to better understand the trade-offs of using a PCB that has utilized a ferromagnetic. Ferromagnetic materials are commonly used for several applications, many of which utilize a magnetic bias to induce the desired phenomenon. Isolators and circulators use a circular ferromagnetic cavity with a bias to induce a single-direction, circular mode. This mode will allow fields to only pass in one direction around the cavity, such that some ports are isolated from others. These magnetic biases can also be used as a form of memory, where the hysteresis curve can store information about a previously applied field. This could be a desired trait, like in a permanent magnet, or undesired like in an electric motor. While bandwidth and miniaturization will be possible with a ferromagnetic introduced into the substrate, these phenomena will potentially occur and harm the antenna's performance, especially when enough power is applied to invoke hysteresis. The other goal of these measurements is to understand the possible drawbacks of the use of magneto-dielectric PCBs for use in a patch antenna.

5.1 MAGTREX 555 Magneto-Dielectric substrate

While there are plenty of attempts at experimentally verifying Hansen's analysis using various ferromagnetic materials, this will be the first one to use a commercial, off-the-shelf PCB with conventional fabrication techniques. Doing so will help control the material's properties thanks to industry standardized material testing, and will also verify the practicality of using this new kind of material in a customary setting. Many attempts at verifying Hansen's paper up to this point have met with limitations in material, fabrication, and measurement capabilities, and this investigation will not. Rogers MAGTREX 555 substrate was used for this experiment along with some Rogers 3006 as a control as it has a near-identical permittivity. While the MAGTREX is 60 mil thick, due to supply chain issues the closest available thickness for 3006 was only 50 mil.

MAGTREX is reported to have a $\mu_r = 6.0$ and $\epsilon_r = 6.5$ in the x/y directions, and an $\epsilon_r = 5.3$ in the z-direction. The dielectric loss tangent is 0.01, while the magnetic loss tangent is less than 0.05 over the range of operation. Rogers reports a useable range up to 500 MHz, after which the magnetic loss becomes too great for many applications, antennas included. In [48] is shown that the characteristic impedance of a patch is inversely proportionate to the loss, meaning that on top of the usual effects of a lossy substrate, the loss here will counteract the gains from the magneto-dielectric. As expected, Rogers reports that for a patch there is still the efficiency bandwidth trade-off, and the size of the antenna will impact the efficiency. Therefore, Rogers recommends that MAGTREX be used as a backing on a two-layered planar antenna or an antenna with an air gap between the antenna and ground plane. Rogers states that in these cases the antenna's efficiency, bandwidth, and z-miniaturization will all be positively influenced. However, for power testing, the patch antenna will suffice, and by not including another material the effects of the ferromagnetic should be better highlighted.

5.2 Antenna Design and Fabrication

5.2.1 Patch Antennas

The front end used for these measurements is nearly the same for the previous chapter except that the desired operating frequency was 400 MHz. Therefore, both patches were designed to operate at 400 MHz, with a 9"x"12 ground plane. A coaxial feed was used for both patches, to isolate the radiation behavior of the patch and not include that of a co-planar feed line as well. A $\frac{W}{L} < 1$ was chosen to prevent two modes from radiating on top of one another and to keep the second mode away from the band of operation of the front end. The ratio was not too near one as this could drastically affect bandwidth and complicate fabrication. The cavity model,

$$f_{res} = \frac{c}{2\sqrt{\epsilon_r \mu_r}} \sqrt{\left(\frac{m}{h}\right)^2 + \left(\frac{n}{L}\right)^2 + \left(\frac{p}{W}\right)^2} \tag{5.2}$$

was used to estimate a resonant frequency for each substrate as in [46], but including μ_r for the magneto-dielectric. The coax feed was then tuned to resonate precisely at 400 MHz and with an input resistance of nearly 50Ω. The results of the tuning are shown in Figures 5.2 and 5.3. There was also an issue of deciding the proper magnetic loss tangent to use in simulation, as the datasheet from Rogers says that the loss will be $\delta < 0.05$. In Figure 5.1 the change in realized gain between difference losses was examined. Not only does the overall maximum change in magnitude, but in frequency as well. This means that it is important to characterize the material on hand before making too precise of a design, as both the operating frequency and the realized gain will change. Based on measurements and the realized gain of the 3006, a loss tangent of 0.01 was assumed for this work.

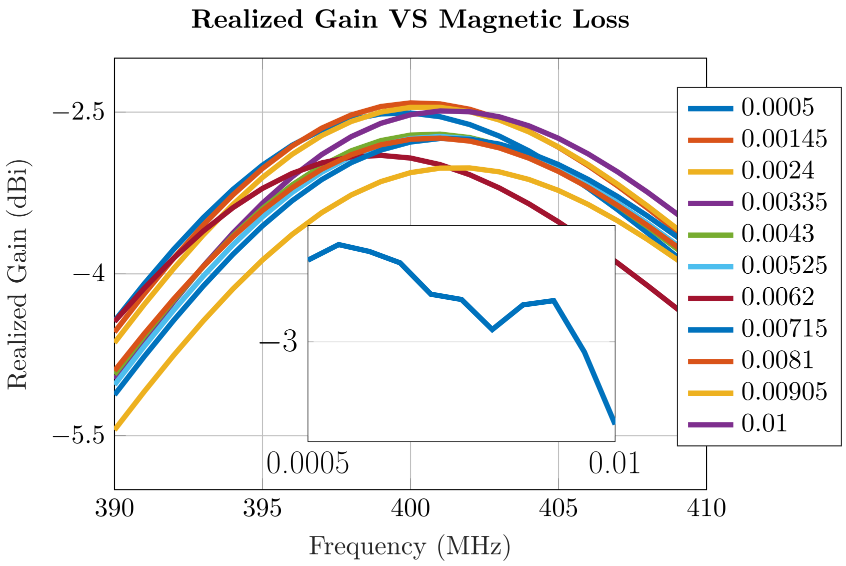

Figure 5.1: Simulated results of various realized gains.

The patches were fabricated using an LPKF S104 mill to drill the coax feed and fiducials. Then a photolithography process was used to etch out the patch patterns on both of the substrates. There was one difference in patch manufacturing. As the MAGTREX patch was smaller, the mill was allowed to partially rub out the patch so that no human error would be introduced in aligning a mask. The 3006 patch was not partially rubbed out and only used etchant for the pattern. Judging by the response of the fabricated patches in Figures 5.2 and 5.3, it would seem that neither is significantly better than the other as they suffered nearly the same percent error in operational frequency with negligible effects on bandwidth. It would be recommended in the case of an antenna with a via a feed of some kind to just use photolithography as the extra work yielded no improvements and risks roughness on

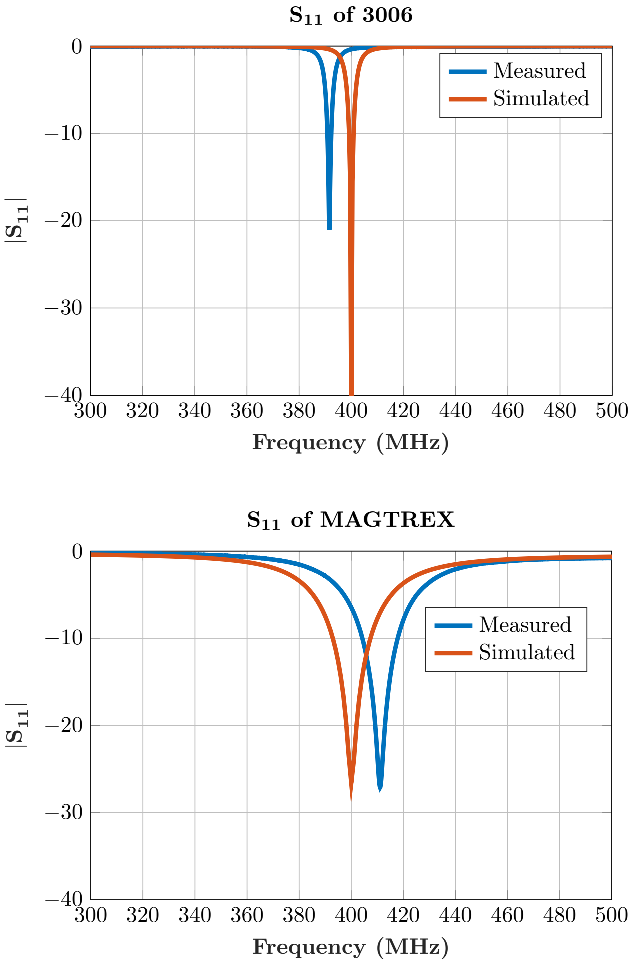

Figure 5.2: Simulated versus measured S-Parameter response of the AUTs.

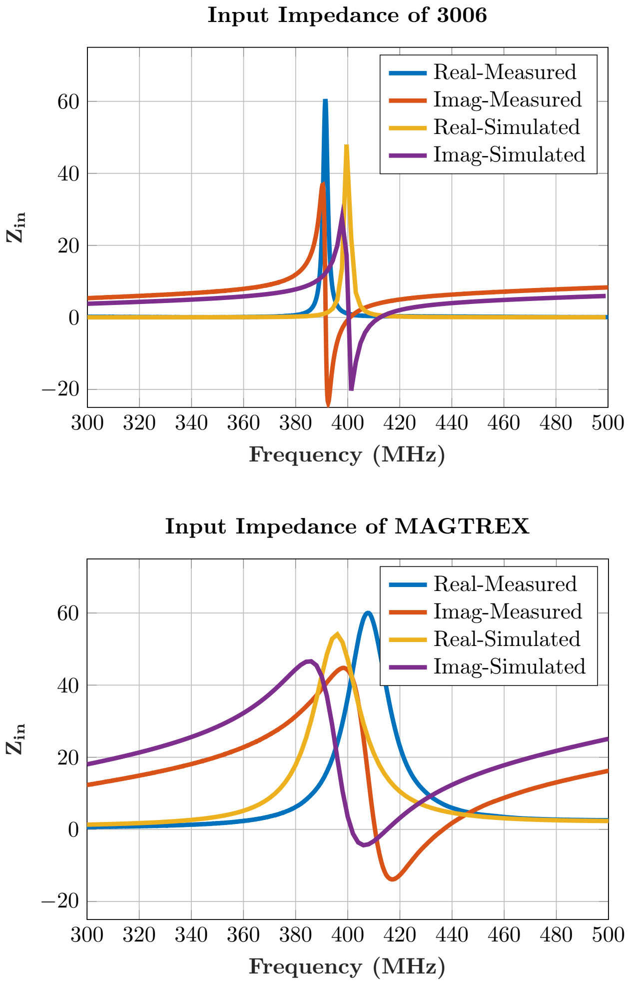

Figure 5.3: Simulated versus measured input impedance response of the AUTs.

the copper's edge - at least at these frequencies. The case of finer details may require milling as human error in aligning vias and fiducials could be too great. There is one improvement, however, and that would be to attempt to compensate for stretching in the printing of the mask. As the mask is printed by a Canon Pixma Pro 100 there is a slight error introduced in the form of lengthening along the axis that the printer is rolling the mask. A large mask, like that of a patch using an entire 9"x12" board, can cause the patch to look longer than it should. This is likely the reason for the shift down in frequency on the 3006 patch. Additionally, this can cause fiducials to become slightly misaligned as well. It is customary to add the height of the substrate to the geometry on the mask to compensate for over-etching, but perhaps with larger structures, this should be neglected on edges that are perpendicular to the longer side of the mask when they are separated by a significant distance. Moving fiducials closer to one another can remove the error in the alignment of the mask after milling. The increase in the frequency of the MAGTREX is most likely due to the mill cutting the exact dimensions and the etchant then removing from the sides slightly, despite efforts made to insulate the entire patch from the etchant through the use of Kapton tape. Despite these minor fabrication errors, the patches are well within tolerances to be used for measurements.

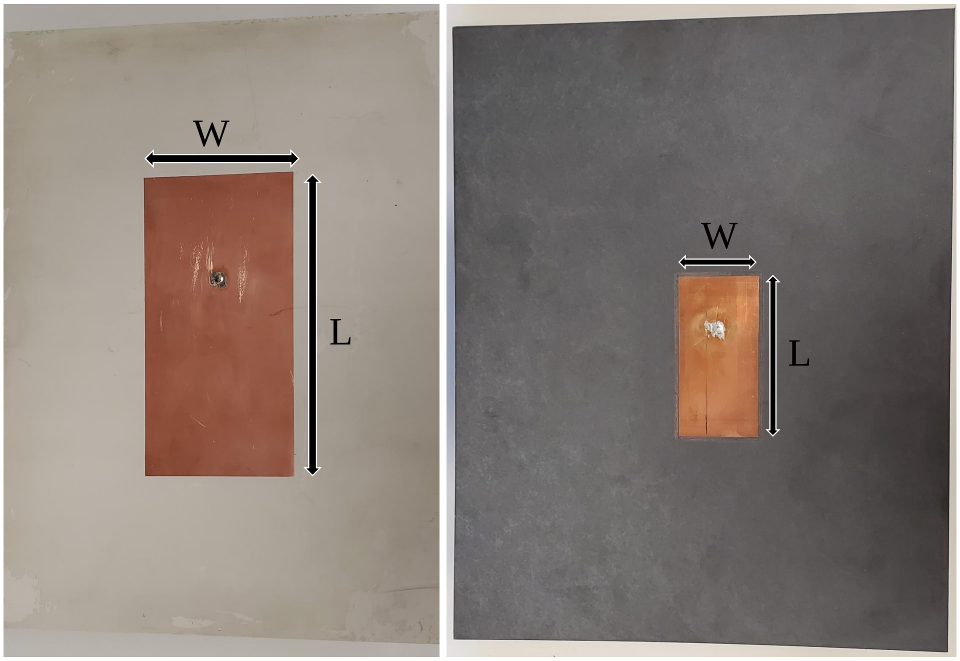

(a) (b)

Figure 5.4: Pictures of the fabrication results. For the 3006 (left) the dimensions are L = 152 mm and W = 76 mm, and the feed is centered in W and 53 mm from the top of the patch. The MAGTREX (right) dimensions are L = 74.6 mm and W = 37.3 mm, and the feed is centered about W and is 24 mm from the top of the patch.

5.2.2 Low Pass Filter

Like with previous measurements, this front will also need a low pass filter that can withstand high input powers. Again, Rogers 3003 was used, and the same g coefficients were used as well. All that was needed was to rescale the filter to cut off at a much lower frequency, in this case, 450 MHz. One more drawback to this filter that was not a problem at higher frequencies was the size of the filter. Without meandering the filter, in simulations, was 20.3 cm long and 6.4 cm wide. The length would make it frustrating to fit it between components, so it was meandered. This reduced the length to 12.7 cm, so placing it between components in the front end wouldn't require as much space to be reserved just for the filter.

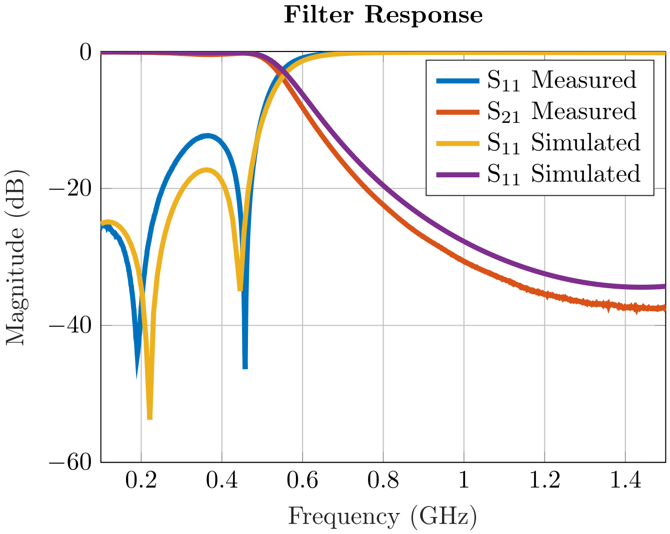

(a)

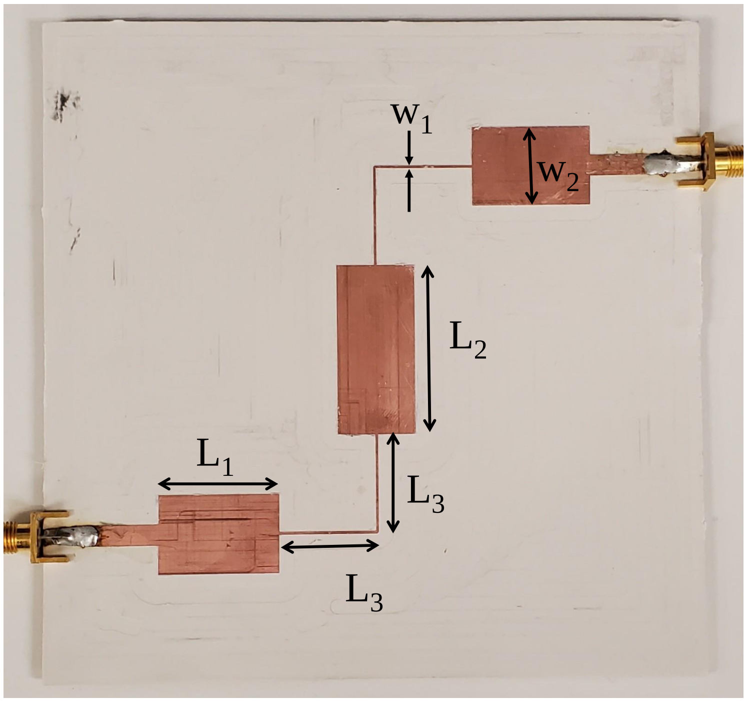

(b)

Figure 5.5: The simulated and measured response of the 400 MHz filter and the fabrication results where $\mathrm{L}_1 = 23\mathrm{mm}, \mathrm{W}_1 = .51, \mathrm{L}_2 = 33\mathrm{mm}, \mathrm{W}_2 = 15.42,$ and $\mathrm{L}_3 = 19\mathrm{mm}$

5.3 Experiment Setup

The measurement setup for this has an identical block diagram as shown again in Figure 5.6. The primary difference, as mentioned before, is it operates around 400 MHz. The instruments are the same, but the passive devices and amplifiers are different. The amplifier is a Mini-circuits ZHL-20W-13+, that then feeds into port 1 of an RFCI CR6153B circulator. The circulator's second port then feeds into a stepped impedance filter to prevent harmonic distortion from the amplifier, and that then feeds into a Mini-circuits ZGBDC30-372HP+ bi-directional coupler. Otherwise, the system is arranged and operated exactly as in Chapter 4. The other difference was the inclusion of one Satimo SH 200 standard gain horn for operation at the UHF band and the BW-N30W20+ attenuator is now on the third port of the circulator. In addition to the measurement setup, the configurations used are also identical, except that instead of replacing the standard gain horn with three smaller ones, just the Satimo SH 200 was used, as it covers the entire band. There was not a second horn to operate in this band for calibration, so the loss had to be measured in the cables and bulkhead separately and added in later.

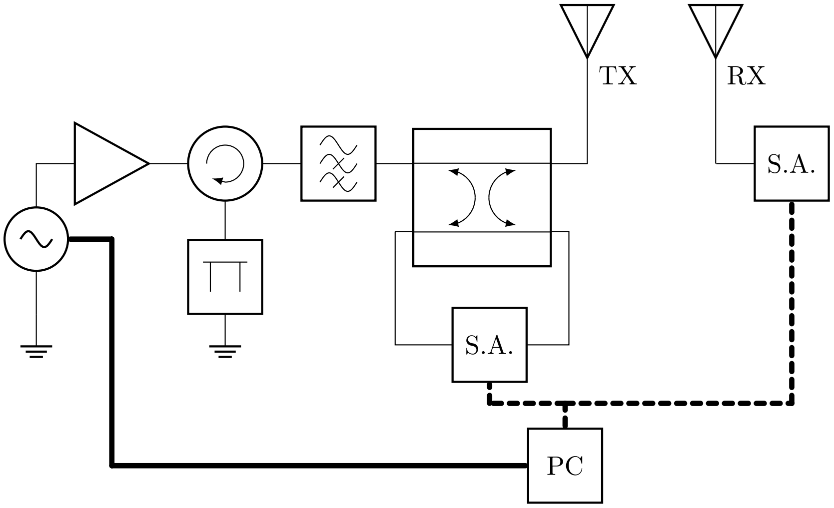

Figure 5.6: Block diagram from the front end used for the experiment.

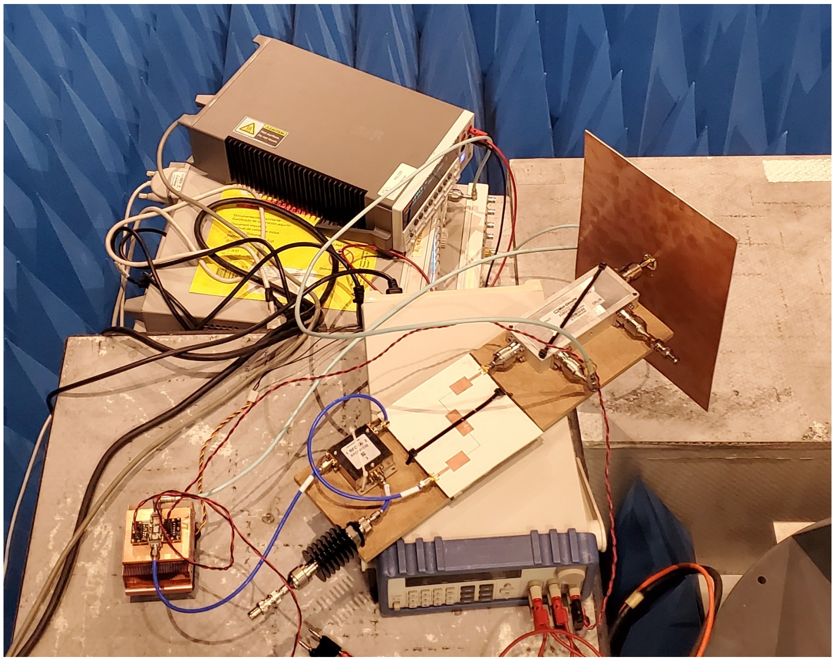

Figure 5.7: Picture of the setup used to measure patch reflection.

5.4 Measurements

5.4.1 Reflection

The MAGTREX patch is expected to detune as the input power increases, as it is well known that due to hysteresis the RF signal will bias the ferromagnetic material as it is incident the patch. The results of measuring the S_{11} under various powers show that the MAGTREX does begin to detune after a certain power. The threshold under which it operates as expected coincides with the hysteresis curve of the material. Once the MAGTREX begins to require a significant amount of power to move along the IV curve, the operational frequency drops in frequency. Also, the bandwidth shrinks slightly and the passband minimum increases by almost 15 dB. The MAGTREX reached a measured temperature of 70^oC, implying that some nonlinearity could be due to thermal energy. There are some issues with this measurement, unfortunately. An infrared (IR) thermometer was used, but the patch was able to interfere with the temperature measurement such that the operating temperature could not be captured while it was on. The measurement here was taken with the IR thermometer pointed right at it, and then the amplifier was turned off, and shortly after the thermometer would begin reading the temperature. However, with how thin the copper was it would be cooling rapidly such that by the time a consistent, averaged temperature was read it would be much cooler. The patch did become hot enough that solder was observed to become soft enough to be scratched with a scrap piece of substrate, left over flux on the connector oxidized, and the alloy within the copper anodized very slightly. These observations indicate that it very easily could have been a few dozen degrees hotter and that it could become hot enough that connections would be in danger after prolonged operation. Despite having an increase of almost 20 dB of S_{11} at the initial center frequency, the wideband and incredible reflection greatly alleviated this issue. Overall, the MAGTREX has a reliable match up to 10 dBW.

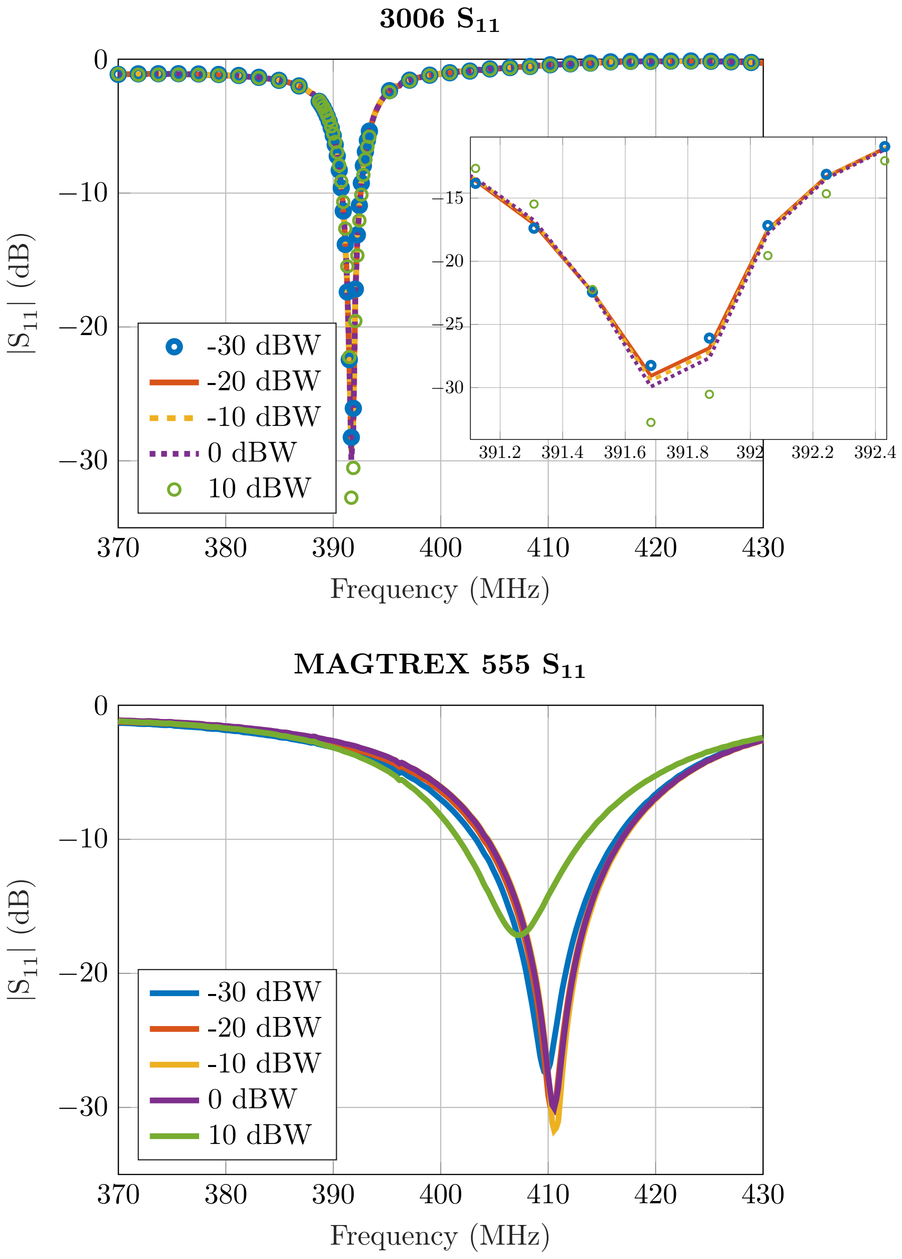

Figure 5.8: S-parameters of the AUTs under power testing.

The change in the match is accompanied by a slight increase in harmonic generation as well. In Figure 5.9 the harmonics within the MAGTREX are compared to that of the 3006. The harmonics within the 3006 are merely a product of the amplifier, as it is known that the amplifier will be generating some small harmonic distortion despite the filtering. The MAGTREX shows a consistently higher harmonic generation, and with the evidence in Figure 5.8 it can be concluded that this is some excess harmonic generation from the MAGTREX's ferromagnetic material. However, all these harmonics are very small, even with the addition of the harmonic distortion from the MAGTREX.

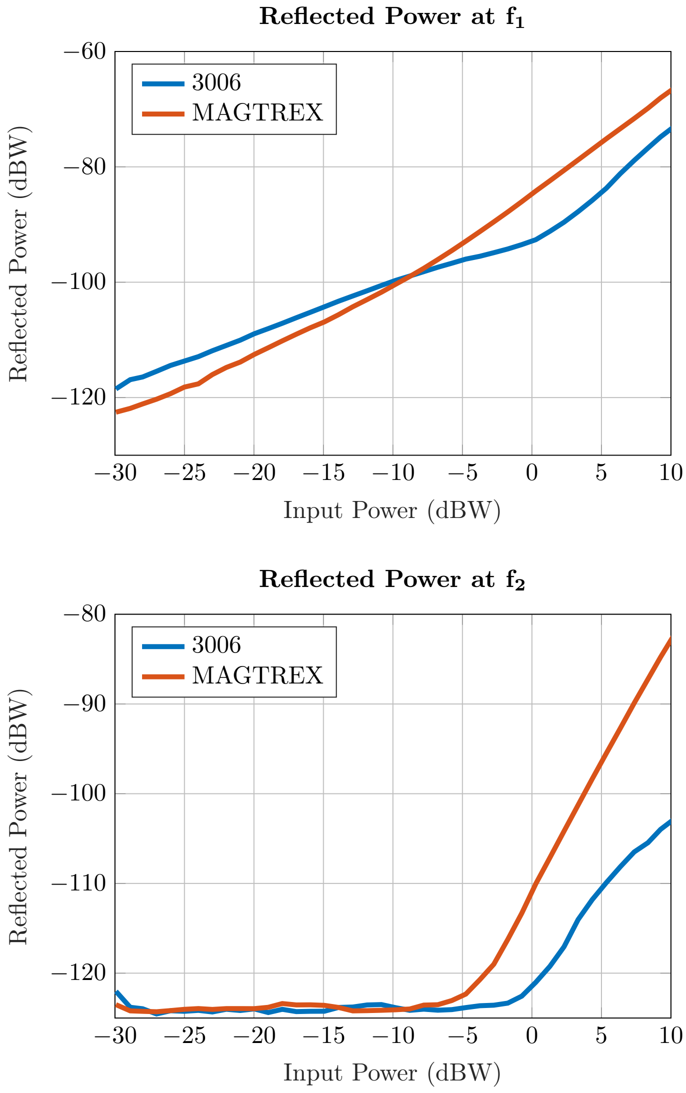

Figure 5.9: S-parameters of the AUTs under power testing.

5.4.2 Radiation

While there is some change to the reflection across power, there seems to be very little harmonic generation in the MAGTREX patch as shown in 5.10. There is little difference between the harmonics in the 3006 and the MAGTREX, indicating that the harmonics present in that measurement are a product of the amplifier and not the MAGTREX behaving nonlinearly.

One explanation is the MAGTREX's loss at these frequencies is perhaps aiding in filtering, just as in [25]. If a ferromagnetic material is to be used at higher powers, it would be far more desirable to use them closer to their cutoff frequency such that the harmonic components would naturally be filtered by the loss at those frequencies. Also, like with the RRELSA, Figure 5.11 shows that the MAGTREX operating as a receive antenna is not affected as the power level is too low due to propagation loss. The only concerning element of Figure 5.11 is the slight asymmetry in the pattern. This comes from the asymmetry in the ground plane, as the patch itself is slightly off-center resulting in the edge currents having a varying degree of influence on the pattern based on what side is being observed.

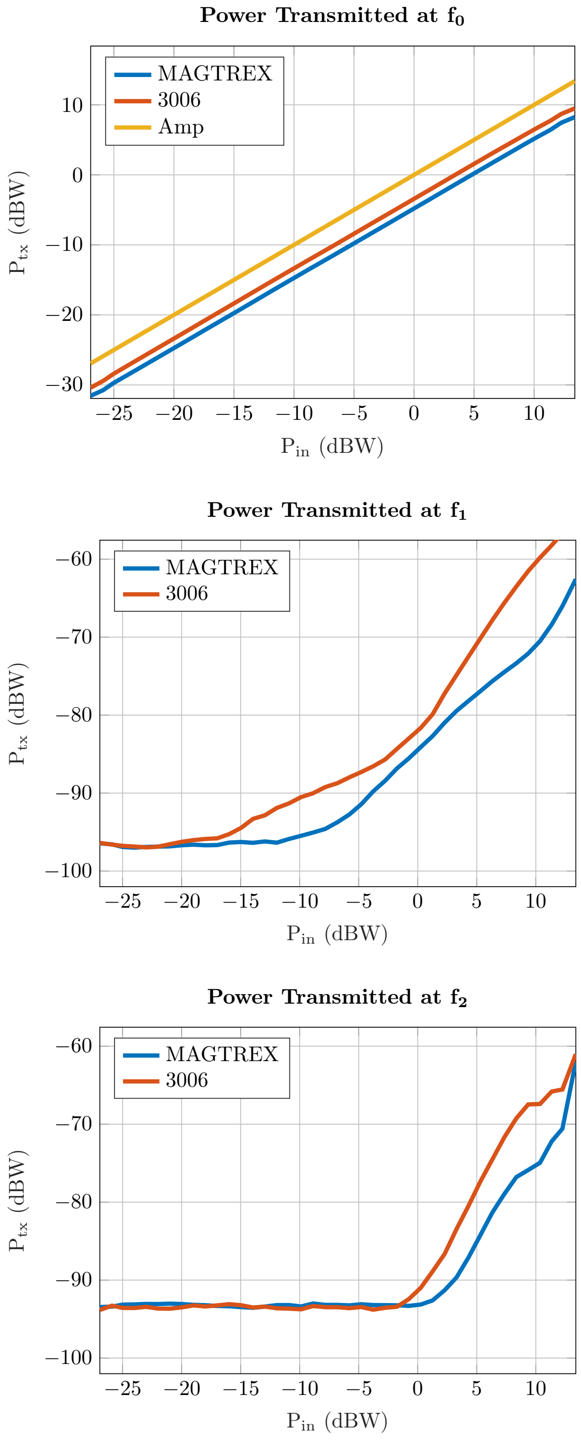

Figure 5.10: Transmitted harmonics of the AUTs.

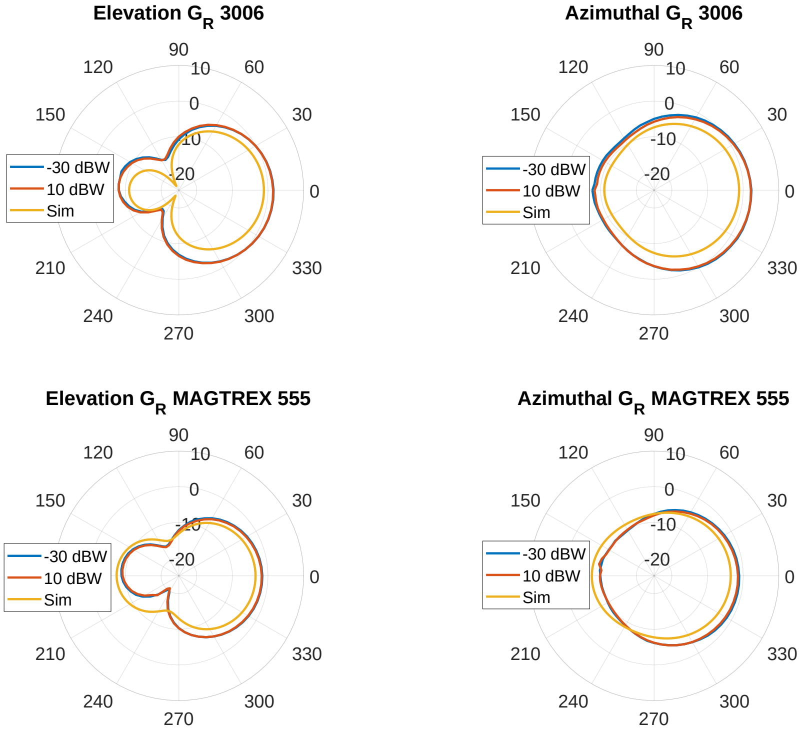

Figure 5.11: Gain patterns of the AUTs under power.

5.5 Concluding Remarks

Magnetic materials have well-known nonlinear characteristics due to their hysteresis curve. Their penchant for collecting magnetic energy in the form of a hysteretic bias can be used to break reciprocity and generate harmonics. It has been shown that the nonlinear characteristics of the MAGTREX 555 substrate can manifest as degradation in antenna performance, albeit only slightly in the case of this particular substrate. A designer needs to consider the operating power levels of an application before using this seemingly ideal improvement on the classic patch antenna. Fortunately, the rapid increase in loss of the material does well to protect it from a loss in power as it is distributed to other frequencies. However, as improvements are made to this material and its cutoff frequency due to magnetic loss is increased proper steps to mitigate the increase in harmonics must be taken. It is then recommended that such an antenna be operated at lower frequencies, such as receiver-only applications, or be operated close to their cutoff frequency to leverage the natural attenuation of the material.

Chapter 6

Future Work and Conclusion

6.1 Future Work

There is a multitude of avenues to continue this work. Firstly, there are still a few other elements to Xfdtd that could be examined, particularly the SPICE modeling. If that system works well enough, then nearly any component could be modeled directly in a full-wave solver. Second, there is still work to be done in characterizing reconfigurable antenna technique trade-offs. Most importantly a refined version of the RRELSA herein needs to be fabricated to examine the harmonic behavior of an efficient varactor-based antenna. Also, only one varactor-based antenna and one mechanical-based antenna were examined. To better understand the nonlinear behavior of varactor-based tuning it would help to look at another antenna in this category. A classic example would be a tunable patch antenna, with varactors on either side across the radiating patches. This would not only corroborate the findings with the RRELSA but could also serve as a testing ground for further varactor-based tuning strategies. It is known that various topologies can be used to minimize power dissipation in varactors, and the patch antenna's simple geometry would lend well to experimenting with this application for antennas. Additionally, testing different sized RRELSAs tuned to the same frequency would allow comparing the effects of DC bias voltage on nonlinear behavior. The MAGTREX could also use some further testing in practical situations, like noise temperature and distortion due to hysteresis. Better characterization of the hysteresis of the material would immensely in design procedures too. This can help inform how to best deal with ferromagnetic substrates near or above ideal power limits, and how to mitigate the issues that arise. Producing a better method of measuring the thermal dissipation of the MAGTREX would help in this avenue as well. Also, redesigning a MAGTREX patch to operate at or below 200 MHz would allow the examination of harmonics at frequencies below the lossy behavior of the substrate. This can isolate the origin of the reduced harmonic distortion.

6.2 Conclusion

There is plenty still to do, however, the work herein has given antenna engineers a better grasp on the effects of making the linear assumption too often. A review of current non-LTI simulation methods helps to inform how to best investigate and design around non-LTI antennas. A new power balance relation and literature review warns antenna engineers looking to better characterize or utilize reactive power generated by nonlinear or time-varying resistances. Power testing of frequency-agile antennas helps to quantify the limitations of reconfigurable antennas that risk nonlinear behavior, which can otherwise be great solutions to communication problems. Finally, power testing of CoTS magneto-dielectric serves to verify theoretical bandwidth gains of such material and to quantify the impact of a ferromagnetic material used in antenna design. In conclusion, it has been shown that removing the LTI assumption from antenna engineering can both help in designing rugged antenna systems, that would otherwise limit the utility of these antennas.

References

[1] H. Hertz, “Ueber strahlen electrischer kraft,” *Annalen der Physik*, vol. 272, no. 4, pp. 769–783, 1889.

[2] M. Manteghi, “Fundamental limits, bandwidth, and information rate of electrically small antennas: Increasing the throughput of an antenna without violating the thermodynamic Q-factor,” *IEEE Antennas and Propagation Magazine*, vol. 61, no. 3, pp. 14–26, 2019.

[3] S. Sankaran, P. Reynaert, and S. Amakawa, “Session 23 overview: THz circuits and front-ends RF subcommittee,” in *2021 IEEE International Solid-State Circuits Conference (ISSCC)*, IEEE, vol. 64, 2021, pp. 322–323.

[4] P. Loghmannia and M. Manteghi, “Broadband parametric impedance matching for small antennas using the Bode-Fano limit,” *arXiv preprint arXiv :1907.11683*, 2019.

[5] K. Schab, D. Huang, and J. J. Adams, “An energy-synchronous direct antenna modulation method for phase shift keying,” *IEEE Open Journal of Antennas and Propagation*, vol. 1, pp. 41–46, 2020.

[6] W. Yao and Y. Wang, “Direct antenna modulation-a promise for ultra-wideband (UWB) transmitting,” in *2004 IEEE MTT-S International Microwave Symposium Digest (IEEE Cat. No. 04CH37535)*, IEEE, vol. 2, 2004, pp. 1273–1276.

[7] A. Shlivinski and Y. Hadad, “Beyond the Bode-Fano bound: Wideband impedance matching for short pulses using temporal switching of transmission-line parameters,” *Physical review letters*, vol. 121, no. 20, p. 204 301, 2018.

[8] A. Kord, D. L. Sounas, and A. Alù, “Achieving full-duplex communication: Magnetless parametric circulators for full-duplex communication systems,” *IEEE Microwave Magazine*, vol. 19, no. 1, pp. 84–90, 2017.

[9] X. Wu, X. Liu, M. D. Hickle, D. Peroulis, J. S. Gómez-Dıaz, and A. Á. Melcón, “Isolating bandpass filters using time-modulated resonators,” *IEEE Trans. Microw. Theory Techn.*, vol. 67, no. 6, pp. 2331–2345, 2019.

[10] M. Salehi and M. Manteghi, “Bandwidth enhancement using nonlinear inductors,” in *2011 IEEE International Symposium on Antennas and Propagation (APSURSI)*, IEEE, 2011, pp. 814–816.

[11] A. Taflove and S. C. Hagness, *Computational Electrodynamics: The Finite-Difference Time-Domain Method*. Artech house, 2005.

[12] S. D. Gedney, “Introduction to the finite-difference time-domain (FDTD) method for electromagnetics,” *Synthesis Lectures on Computational Electromagnetics*, vol. 6, no. 1, pp. 1–250, 2011.

[13] N. V. Kantartzis and T. D. Tsiboukis, “Higher order FDTD schemes for waveguide and antenna structures,” *Synthesis Lectures on Computational Electromagnetics*, vol. 1, no. 1, pp. 1–226, 2005.

[14] S. A. Maas, *Nonlinear Microwave and RF Circuits*. Artech House, 2003.

[15] S. Bass, A. Palmer, K. Schab, K. Kerby-Patel, and J. Ruyle, “Conversion matrix method of moments for time-varying electromagnetic analysis,” *arXiv preprint arXiv:2103.06135*, 2021.

[16] C.-C. Huang and T.-H. Chu, “Analysis of wire scatterers with nonlinear or time-harmonic loads in the frequency domain,” *IEEE transactions on antennas and propagation*, vol. 41, no. 1, pp. 25–30, 1993.

[17] P. Jayathurathnage, F. Liu, M. S. Mirmoosa, X. Wang, R. Fleury, and S. A. Tretyakov, “Time-varying components for enhancing wireless transfer of power and information,” *Physical Review Applied*, vol. 16, no. 1, p. 014 017, 2021.

[18] J. M. Manley and H. E. Rowe, “Some general properties of nonlinear elements-part I. general energy relations,” *Proceedings of the IRE*, vol. 44, no. 7, pp. 904–913, 1956.

[19] V. G. Smith, “Reactive and fictitious power,” *Transactions of the American Institute of Electrical Engineers*, vol. 52, no. 3, pp. 748–751, 1933. DOI: 10.1109/T-AIEE.1933.5056390.

[20] J. T. Bernhard, “Reconfigurable antennas,” *Synthesis lectures on antennas*, vol. 2, no. 1, pp. 1–66, 2007.

[21] Y. Zheng, A. Hristov, A. Giere, and R. Jakoby, “Suppression of harmonic radiation of tunable planar inverted-F antenna by ferroelectric varactor loading,” in *2008 IEEE MTT-S International Microwave Symposium Digest*, IEEE, 2008, pp. 959–962.

[22] J.-B. Yan, S. Yong, and J. T. Bernhard, “Intermodulation and harmonic distortion in frequency reconfigurable slot antenna pairs,” *IEEE Transactions on Antennas and Propagation*, vol. 62, no. 3, pp. 1138–1146, 2013.

[23] K. Buisman, C. Huang, P. J. Zampardi, and L. C. de Vreede, “RF power insensitive varactors,” *IEEE microwave and wireless components letters*, vol. 22, no. 8, pp. 418–420, 2012.

[24] R. Hansen and M. Burke, “Antennas with magneto-dielectrics,” *Microwave and optical technology letters*, vol. 26, no. 2, pp. 75–78, 2000.

[25] Z. Zheng and X. Wu, “A miniaturized UHF Vivaldi antenna with tailored radiation performance based on magneto-dielectric ferrite materials,” *IEEE Transactions on Magnetics*, vol. 56, no. 3, pp. 1–5, 2020.

[26] K. F. F. Farzami and M. Norooziarab, “Miniaturization of a microstrip antenna using a compact and thin magneto-dielectric substrate,” *IEEE Antennas and Wireless Propagation Letters*, vol. 10, pp. 1540–1542, 2011. DOI: 10.1109/LAWP.2011.2181968.

[27] K. Yee, “Numerical solution of initial boundary value problems involving Maxwell’s equations in isotropic media,” *IEEE Transactions on antennas and propagation*, vol. 14, no. 3, pp. 302–307, 1966.

[28] T. Namiki, “3-D ADI-FDTD method-unconditionally stable time-domain algorithm for solving full vector Maxwell’s equations,” *IEEE Transactions on Microwave Theory and Techniques*, vol. 48, no. 10, pp. 1743–1748, 2000. DOI: 10.1109/22.873904.

[29] J. Meixner, “The behavior of electromagnetic fields at edges,” *IEEE Transactions on antennas and propagation*, vol. 20, no. 4, pp. 442–446, 1972.

[30] J.-P. Berenger, "Improved PML for the FDTD solution of wave-structure interaction problems," *IEEE transactions on Antennas and Propagation*, vol. 45, no. 3, pp. 466–473, 1997.

[31] J. A. Roden and S. D. Gedney, "Convolution PML (CPML): An efficient FDTD implementation of the cfs–pml for arbitrary media," *Microwave and optical technology letters*, vol. 27, no. 5, pp. 334–339, 2000.

[32] S. Bass, "Non-LTI antenna design and modeling techniques," 2022.

[33] A. E. Knowlton, "Reactive power concepts in need of clarification," *Transactions of the American Institute of Electrical Engineers*, vol. 52, no. 3, pp. 744–747, 1933. DOI: 10.1109/T-AIEE.1933.5056389.

[34] IEEE, "IEEE standard definitions for the measurement of electric power quantities under sinusoidal, nonsinusoidal, balanced, or unbalanced conditions," 2010.

[35] A. Emanuel, "Summary of IEEE standard 1459: Definitions for the measurement of electric power quantities under sinusoidal, nonsinusoidal, balanced, or unbalanced conditions," *IEEE Transactions on Industry Applications*, vol. 40, no. 3, pp. 869–876, 2004. DOI: 10.1109/TIA.2004.827452.

[36] L. S. Czarnecki, "What is wrong with the Budeanu concept of reactive and distortion power and why it should be abandoned," *IEEE Transactions on Instrumentation and Measurement*, vol. IM-36, no. 3, pp. 834–837, 1987. DOI: 10.1109/TIM.1987.6312797.

[37] K. Yumak and O. Usta, "A controversial issue: Power components in nonsinusoidal single-phase systems," in *2011 7th International Conference on Electrical and Electronics Engineering (ELECO)*, 2011, pp. I-157-I–161.

[38] W. V. Lyon, "Reactive power and power factor," *Electrical Engineering*, vol. 52, no. 5, pp. 342–342, 1933. DOI: 10.1109/EE.1933.6430731.

[39] M. E. Balci and M. H. Hocaoglu, "Quantitative comparison of power decompositions," *Electric Power Systems Research*, vol. 78, no. 3, pp. 318–329, 2008.

[40] N. LaWhite and M. D. Ilic, "Vector space decomposition of reactive power for periodic nonsinusoidal signals," *IEEE Transactions on Circuits and Sys-*

tems I: Fundamental Theory and Applications, vol. 44, no. 4, pp. 338–346, 1997.

[41] L. S. Czarnecki, "Considerations on the reactive power in nonsinusoidal situations," *IEEE transactions on instrumentation and measurement*, no. 3, pp. 399–404, 1985.

[42] W. R. Bennett, "New results in the calculation of modulation products," *The Bell System Technical Journal*, vol. 12, no. 2, pp. 228–243, 1933. DOI: 10.1002/j.1538-7305.1933.tb03224.x.

[43] L. Szolc, T. Poydence, and J. Ruyle, "Frequency-agile ring resonator end-loaded slot antenna," *Microwave and Optical Technology Letters*, vol. 59, no. 8, pp. 1876–1882, 2017.

[44] A. Bauer, "External quality factor in antennas and their use in filtenna design," 2022.

[45] D. M. Pozar, *Microwave Engineering*. John wiley & sons, 2011.

[46] C. A. Balanis, *Antenna Theory: analysis and design*. John wiley & sons, 2016.

[47] J. Dobrick, "Magneto-dielectric materials enable antenna miniaturization," *Antenna Applications Symposium*, vol. 46, 2021.

[48] C. Niamien, S. Collardey, A. Sharaiha, and K. Mahdjoubi, "Compact expressions for efficiency and bandwidth of patch antennas over lossy magneto-dielectric materials," *IEEE Antennas and Wireless Propagation Letters*, vol. 10, pp. 63–66, 2011.